Intracortical injection of immune checkpoint inhibitor promotes monocyte/macrophage infiltration and restores microglial function and neuronal activity in an AD mouse model

Taeyoung Park[1,2,3], Leechung Chang[4,5], Seung Won Chung[1,2,3], Seowoo Lee[1,2,3], Sungjun Bae[6], Carlo Condello[7,8], Yong Ho Kim[1,2,6,9,10,11,12], Jaecheol Lee[6,9,11,12,13,14,15], Han-Joo Kim[6], Ho-Keun Kwon[4,5,16,*] and Minah Suh[1,2,3,6,9,17,18,*]

[1]Department of Biomedical Engineering, Sungkyunkwan University, Suwon 16419, Republic of Korea
[2]Center for Neuroscience Imaging Research (CNIR), Institute for Basic Science (IBS), Suwon 16419, Republic of Korea
[3]Department of Intelligent Precision Healthcare Convergence (IPHC), Fourth Stage of Brain Korea 21 Project (BK 21), Suwon 16419, Sungkyunkwan University, Republic of Korea
[4]Department of Microbiology and Immunology, Yonsei University College of Medicine, Seoul 03722, Republic of Korea
[5]Institute for Immunology and Immunological Diseases, Yonsei University College of Medicine, Seoul 03722, Republic of Korea
[6]IMNEWRUN Inc., Suwon 16419, Republic of Korea
[7]Institute for Neurodegenerative Diseases, University of California San Francisco, San Francisco, CA, USA
[8]Department of Neurology, University of California San Francisco, San Francisco, CA, USA
[9]Biomedical Institute for Convergence at SKKU (BICS), Sungkyunkwan University, Suwon 16419, Republic of Korea
[10]SKKU Advanced Institute of Nanotechnology (SAINT), Sungkyunkwan University, Suwon 16419, Republic of Korea
[11]Department of Nano Science and Technology, Sungkyunkwan University, Suwon 16419, Republic of Korea
[12]Department of Nano Engineering, Sungkyunkwan University, Suwon 16419, Republic of Korea
[13]School of Pharmacy, Sungkyunkwan University, Suwon 16419, Republic of Korea
[14]Department of Biopharmaceutical Convergence, Sungkyunkwan University, Suwon 16419, Republic of Korea
[15]Department of Biohealth Regulatory Science, Sungkyunkwan University, Suwon 16419, Republic of Korea
[16]Brain Korea 21 PLUS Project for Medical Sciences, Yonsei University College of Medicine, Seoul 03722, Republic of Korea
[17]KIST-SKKU Brain Research Center, Suwon 16419, Republic of Korea
[18]Samsung Advanced Institute for Health Science & Technology (SAIHST), Sungkyunkwan University, Suwon 16419, Republic of Korea
[*]Correspondence and requests for materials should be addressed to H.K.K. (HK@yuhs.ac) or to M.S. (minahsuh@skku.edu).

Abstract

Understanding the intricate interplay among immune responses and homeostatic cell function in Alzheimer's disease (AD) remains challenging. Here, we present a novel strategy to mitigate AD pathology by directly modulating the immune checkpoint PD-1/PD-L1 signaling pathway in the brain, where elevated levels of microglial PD-1 and astrocytic PD-L1 have been observed. We found that a single intracortical injection of anti-PD-L1 antibody facilitates the infiltration of peripheral immune cells into the brain, including IL-10-secreting Ly6C^{+} monocytes. Subsequently, this leads to the restoration of microglial homeostatic functions including an increase in P2RY12 expression, which enhances microglial process extension. This cascade of events following anti-PD-L1 injection is crucial for regulating abnormally hyperactive neurons and reducing amyloid-beta plaques. These findings suggest that the direct application of immune checkpoint blockade in the brain could offer a new approach to managing the delicate cell-cell interactions among neurons, glial cells, and peripheral immune cells in the AD brain.

Keywords: Alzheimer's disease, immune checkpoint, immunotherapy, microglia, monocytes, neuronal hyperactivity, in vivo two-photon imaging

Main

Alzheimer's disease (AD) is the leading cause of dementia, characterized by the progressive accumulation of amyloid-beta (Aβ) plaques, neurofibrillary tangles, and chronic neuroinflammation, resulting in memory and cognitive decline[1]. Recent evidence suggests the beneficial impact of immunotherapy in AD treatment, particularly using immune checkpoint antibody targeting the programmed cell death protein-1/programmed death-ligand 1 pathway (PD-1/PD-L1) in the periphery[2, 3]. Studies indicate that systemic injection of anti-PD-L1 antibody leads to therapeutic effects in AD mouse models by activating the immune system outside the brain and enhancing the recruitment of infiltrating monocyte-derived macrophages to the brain via the choroid plexus[3]. These infiltrating monocyte-derived macrophages participate in the phagocytosis of Aβ and tau, although the exact mechanisms by which they contribute to this process within the brain are not fully understood. Monocytes and macrophages play a multi-phasic role in the brain, responding to injury initially by aiding in pathogen clearance and debris removal, and subsequently promoting tissue repair and the resolution of inflammation[3, 4]. Under normal conditions, the blood-brain barrier (BBB) restricts peripheral immune cell entry into the central nervous system (CNS), and in several Aβ mouse models it remains mostly intact, limiting immune cell infiltration[5-7]. Studies of the role of monocytes infiltrating the brain in AD underscore their importance in the brain's response to disease and highlight them as potential targets for therapeutic interventions[3, 8-10]. Although recent research emphasizes the role of peripheral immune cells in AD pathology[11, 12], the intricate relationships among these peripheral immune cells, brain intrinsic cells, and the modulation of the PD-1/PD-L1 axis in the brain are yet to be fully elucidated.

Despite PD-1 and PD-L1 being primarily found in peripheral immune cells, emerging research reveals their upregulated expression in the brains of AD patients and AD mouse models[13]. This suggests that targeting PD-1/PD-L1 signaling in the brain could offer a novel therapeutic approach for AD, particularly within brain-resident immune cells like microglia, which express PD-1 and respond to PD-L1 from astrocytes. While the modulation of the PD-1/PD-L1 pathway through the conditional loss of PD-1 in hippocampal excitatory neurons in aged mouse models has led to improved synaptic transmission and cognitive function[14], the specific role of PD-1/PD-L1 in glial cells during AD remains unclear. In AD, microglia can enter a stalled state, characterized by altered gene expression and impaired phagocytosis[15, 16]. An elevated level of PD-1/PD-L1 was also observed in microglia and astrocyte[13]. This state somewhat resembles the sustained expression of PD-1 and PD-L1 observed in exhausted peripheral immune cells, a condition commonly seen in chronic infections and tumors, where it plays a crucial role in suppressing excessive immunopathological responses and preventing tissue damage[17]. In the context of cancer, this chronic expression of PD-1 and PD-L1 contributes to immune escape from the immune cells by tumors, enabling them to persist and grow despite an active immune response[18]. Similarly, in the AD brain, we hypothesize that the chronic activation of PD-1/PD-L1 signaling in glial cells might contribute to the impaired immune surveillance and clearance of neurotoxic substances, such as Aβ plaques. Therefore, targeting microglial signaling pathways, particularly by inhibiting PD-1/PD-L1 signaling, may help treat neurodegenerative diseases by enhancing microglial homeostatic functions and mitigating neuroinflammatory responses.

Restoring the functions of both microglia and neurons is crucial in AD treatment, as it offers a

fundamental approach to address the cognitive decline that is a hallmark of AD. One of the homeostatic functions of microglia is to modulate neuronal activity, including monitoring and inhibiting abnormal neuronal hyperactivity[19-21]. Microglia sense neuronal activity by detecting changes in ATP levels[19]. When ATP levels increase, microglia are attracted to active neurons through the P2RY12 receptor. The subsequent conversion of ATP to ADP and adenosine suppresses neuronal activity by reducing glutamate release and receptor response in a cyclic AMP concentration-dependent manner[19]. In AD patients and several AD animal models, abnormal hyperactivity of cortical and hippocampal neurons correlates with AD-related network dysfunction and cognitive impairments[22-27]. Moreover, the expression of microglial P2RY12 is reduced in AD[28-30], suggesting its potential as a marker for disrupted microglial function in inhibiting hyperactive neurons. However, understanding how AD pathology affects microglia-neuron crosstalk, and how to keep this interaction in a normal state in the context of the complex and diverse mechanisms shaping abnormal neuronal hyperactivity in AD, is challenging.

Here, we investigated the therapeutic effects of the immune checkpoint blockade through a single intracortical injection in the brain of the 5xFAD AD model mice, employing cell profiling and *in vivo* two-photon imaging of microglia and neurons. Targeting PD-1/PD-L1 signaling in the brain led to the evident infiltration of $Ly6C^{+}$ monocytes 1 day after intracortical anti-PD-L1 injection. At 7 days post-injection, it effectively rescued microglial dysfunction and restored neuronal baseline calcium activity in AD, with a significant reduction of Aβ plaques along with increased plaque-associated microglia. Our results provide insights into the therapeutic potential of immune checkpoint blockade within the brain for AD treatment, emphasizing the importance of understanding the specific role of immune checkpoints in brain-resident immune cells and their implications for neuroinflammatory disorders.

Results

Increased expression of glial PD-1 and PD-L1 in the brain of the 5xFAD mouse model

First, we examined the expression levels of PD-1 and PD-L1 in the brains of the 5xFAD and age-matched wild-type (WT) mice. Immunostaining analysis revealed elevated expression levels of PD-1 (Fig. 1a) and PD-L1 (Fig. 1b) throughout various brain regions of 8-month-old 5xFAD mice compared to WT mice. For this study, we focused our attention on measuring the assessed levels of PD-1 and PD-L1 expression in the cortex, a site vulnerable to AD pathology[31], and the subiculum of the hippocampus, an early site of Aβ plaque and tangle formation linked to cognitive decline[32].

Microglia in the 5xFAD mice exhibited a significant increase in PD-1 expression, particularly in the cortex and subiculum (Fig. 1a, c). Co-localization analysis with the microglial marker Iba-1 and the neuronal marker NeuN revealed that PD-1 expression was predominantly elevated in microglia (Fig. 1d, e). Additionally, astrocytes in 5xFAD mice exhibited a significant increase in PD-L1 expression, as indicated by the astrocytic marker glial fibrillary acidic protein (GFAP) (Fig. 1b, f, g). Neurons showed relatively lower expression levels of PD-L1 compared to glial cells (Fig. 1g, h). Our longitudinal analysis of astrocytic PD-L1 expression in 5xFAD mice revealed an age-dependent increase (Fig. 1i, j, n). At 4 months of age, when Aβ levels were low (Fig. 1m), astrocytic PD-L1 and GFAP expression were barely detectable in the cortex (Fig. 1j, k, l, n). However, as disease progression continued, an increase in these markers was noticeable in the cortex (Fig. 1j, k, l, n), highlighting the significant correlation between disease severity and the rise in these glial markers. These findings emphasize the interconnected roles of microglia, astrocytes, and neurons in AD pathology, where microglia help the formation of neurotoxic reactive astrocytes, leading to further neuronal damage[33]. Our data show a strong link between PD-L1 and GFAP expression, suggesting that targeting PD-L1 in astrocytes could disrupt this harmful cycle, potentially restoring microglial and neuronal function.

Intracortical injection of anti-PD-L1 antibody binds to astrocytes and induces peripheral immune cell infiltration

To specifically examine the impact of anti-PD-L1 on the brain, we injected anti-PD-L1 antibody into the right primary somatosensory cortex of the forelimb region (S1FL) in 5xFAD mice to assess the extent of antibody distribution and identify the target cells (Fig. 2a). One day after the injection, immunostaining targeting the rat IgG revealed that the injected anti-PD-L1 was well distributed over the cortical region (approximately 1-1.5 mm^3 in volume), with particularly strong binding to astrocytes expressing GFAP compared to control IgG-injected area (Fig. 2b, Extended Data Fig. 1).

Previous studies demonstrated that systemic anti-PD-L1 administration through intravenous injection activates peripheral immune responses in the choroid plexus and recruits myeloid cells to the CNS[2,3]. In contrast, we sought to investigate the effects of directly modulating the immune checkpoint of glial cells within the brain. Specifically, we used intracortical injection of anti-PD-L1 to determine whether this approach could also promote immune cell infiltration and enhance the brain's local immune response. (Fig. 2c, g). Flow cytometry analysis of cells,

isolated from the injection site of the brain (approximately 1.5 mm^3 in volume), 1 day post-injection, revealed a significant increase in peripherally derived immune cells ($CD45^{high}$ $CD11b^{low}$ lymphocytes and $CD45^{high}$ $CD11b^{high}$ myeloid cells) in the anti-PD-L1-treated area compared to the control IgG-treated area in the same 5xFAD mouse, indicating substantial immune cell infiltration following anti-PD-L1 treatment (Fig. 2d-f). In contrast, WT mice, which do not express high levels of PD-L1, showed no notable immune cell infiltration following anti-PD-L1 treatment (Fig. 2h-j). By 7 days post-injection, the earlier increase in infiltrating immune cells was no longer evident in the anti-PD-L1-treated area, indicating that the infiltration was transient (Extended Data Fig. 2a-c). Moreover, no detectable levels of the injected control IgG or anti-PD-L1 antibodies were found in the brains of 5xFAD mice at 7 days post-injection (Extended Data Fig. 2d). These results suggest that the administered anti-PD-L1 antibody has an immediate effect on local innate cells within the brain tissue but does not impact infiltrating immune cells. These findings underscore the critical role of PD-L1 expression and its modulation within the brain in regulating immune cell infiltration and shaping local immune responses in the 5xFAD mouse model.

Intracortical injection of anti-PD-L1 antibody increases chemokine expression and induces $Ly6C^+$ monocyte/macrophage infiltration

To identify the immune cell types infiltrating the cortex following anti-PD-L1 treatment, we profiled the immune cell populations using multiparameter flow cytometry, comparing the effects of anti-PD-L1 to control IgG injections. We first employed an unbiased uniform manifold approximation and projection (UMAP) analysis to visualize the overall changes in immune populations (Extended Data Fig. 3, Extended Data Fig. 4, Fig. 3a). This analysis revealed a notable increase in immune cells within the anti-PD-L1-treated hemisphere compared to the control IgG-treated hemisphere in the same 5xFAD mouse (Fig. 3b, c, Extended Data Fig. 5). Specifically, a proportional analysis showed a pronounced increase in $Ly6C^+$ monocytes/macrophages (Mo/MΦ) in the anti-PD-L1-treated hemisphere (Fig. 3d, e). Notably, while the infiltration of peripheral monocytes and macrophages was most evident in the anti-PD-L1-treated hemisphere, we must also consider the possible proliferation or activation of brain-resident perivascular macrophages or other CNS-resident immune cells expressing Ly6C. Although the control IgG-injected hemisphere showed minimal monocyte or macrophage presence (Fig. 2d-f, Fig. 3b), the observed increase in $Ly6C^+$ cells could comprise both infiltrating peripheral cells and locally proliferating or activated CNS macrophages. We observed increases in $Ly6C^+$ Mo/MΦ, $CD4^+$ conventional T cells (Tconv) and $CD4^+FOXP3^+$ regulatory T cells (Treg, a non-significant trend towards increase was observed), which play critical immunoregulatory roles (Fig. 3f). Further analysis showed that anti-PD-L1 treatment significantly upregulated chemokines and cytokines like CCL5, CXCL10, CCL22, and IL-12p40, which are linked to enhanced recruitment and infiltration of Mo/MΦ and T cell (Fig. 3g, Extended Data Fig. 6). We stained brain sections for the anti-inflammatory cytokine IL-10 and found that it colocalized by infiltrating $Ly6C/G^+$ monocytes or macrophages only in the brain area treated with anti-PD-L1 (Fig. 3h). These findings suggest that PD-L1 blockade facilitates the recruitment of immunoregulatory cells by enhancing chemokine production, thereby amplifying the immune response and altering the local immune milieu in the brain.

Anti-PD-L1 increases astrocytic TGF-β, microglial P2RY12 expression, and microglial process convergence in 5xFAD mice

To assess the effects of anti-PD-L1 treatment on microglial function, we evaluated P2RY12 levels, a key marker of microglial homeostasis. Immunostaining analysis confirmed a significant reduction in P2RY12 levels in 8-month-old 5xFAD mice compared to age-matched WT mice (Fig. 4a-c), consistent with previous reports in APP mouse models[29, 30]. This reduction was particularly pronounced in plaque-associated microglia, while non-plaque-associated microglia in 5xFAD mice exhibited a less marked reduction in P2RY12 levels compared to WT microglia. Notably, 7 days after anti-PD-L1 treatment, P2RY12 expression was significantly increased compared to control IgG treatment (Fig. 4a-c). Focusing on plaque-associated microglia, we observed that anti-PD-L1 treatment significantly increased the P2RY12-positive area surrounding plaques compared to the control IgG-treated 5xFAD mice (Fig. 4b, Extended Data Fig. 7). This suggests that PD-L1 blockade enhances P2RY12 expression specifically in microglia near plaques, potentially promoting microglial homeostasis in regions heavily impacted by AD pathology. Further analysis using quantitative PCR on astrocytes and microglia isolated by fluorescence-activated cell sorting (FACS) from 8-month-old 5xFAD mice revealed that anti-PD-L1 treatment increased *Tgfβ1* mRNA levels in astrocytes (Fig. 4d, e). Given that TGF-β1 is essential for maintaining consistent P2RY12 expression in microglia[34], it is likely that astrocyte-derived TGF-β1 plays a key role in influencing microglia to restore P2RY12 expression.

To examine microglial homeostatic function utilizing *in vivo* two-photon imaging, we generated mice with fluorescence in microglia in AD brain by crossbreeding 5xFAD mice with CX3CR1-GFP mice (Fig. 4f). Following a focal laser brain tissue injury to induce ATP release, we observed microglial process convergence to the injury site in the cortex (Fig. 4f, g). No differences were found in microglial process convergence in the cortex between the WT group and the WT group with control IgG injection (Fig. 4g-i). However, a significant reduction in microglial process convergence was evident in 5xFAD mice with control IgG injection compared to WT mice (Fig. 4g-i), consistent with previous results[35, 36]. Surprisingly, anti-PD-L1 treatment significantly rescued decreased microglial process convergence in 5xFAD mice (Fig. 4g-i). Considering that microglial responses can vary depending on their proximity to Aβ plaques[37] and the number of plaque-associated microglia, we ensured consistency in experimental conditions by confirming that there was no difference in the number of microglia around the imaging area between the control IgG-treated 5xFAD group and the anti-PD-L1-treated 5xFAD group (Fig. 4j). This finding suggests that the homeostatic function of plaque-associated microglia is indeed restored following anti-PD-L1 injection.

Importantly, we confirmed the functional significance of restored microglial P2RY12 expression by demonstrating the recovery of microglial response to focal injury following anti-PD-L1 treatment in 5xFAD mice. These findings underscore the role of directly engaging PD-L1 blockade within the AD brain in restoring microglial homeostatic function, thereby offering novel insights into the therapeutic potential of anti-PD-L1 therapy in AD.

Anti-PD-L1 restores abnormal spontaneous neuronal hyperexcitability in 5xFAD mice

To assess whether PD-1/PD-L1 blockade affects microglia-neuron crosstalk, specifically microglial negative feedback controlling of neuronal activity in the AD brain[19], we utilized *in vivo* two-photon neuronal calcium imaging. We co-delivered AAV9-CamK2a-GCaMP6f for visualizing excitatory neuronal calcium activity, along with antibody into the cortex of 8-month-old 5xFAD mice (Fig. 5a). The expression of the virus in neurons was confirmed by immunostaining with anti-GFP (Fig. 5b). By imaging GCaMP-positive excitatory neurons, we monitored calcium dynamics and frequencies of spontaneous calcium transients at the single-neuron level.

No significant differences in spontaneous neuronal calcium transients in the WT were found between the sham group and the control IgG injection group indicating a lack of neuronal hyperactivity in these two groups (Fig. 5c-g). Consistent with previous studies[24, 26, 27], an increase in neuronal hyperactivity was observed in the 5xFAD mice. In contrast, anti-PD-L1 injection in the 5xFAD mice resulted in the recovery of hyperexcitable neuronal calcium transients. There was a significant decrease in both the fraction and mean frequency of hyperactive neurons in the 5xFAD mice with anti-PD-L1 injection. This observation suggests that PD-1/PD-L1 blockade may play a regulatory role in restoring microglial homeostasis, thereby reshaping microglia-neuron crosstalk and reducing neuronal hyperactivity, a hallmark of AD pathology.

Anti-PD-L1 promotes microglial phagocytosis of Aβ in 5xFAD mice

We investigated the effects of anti-PD-L1 intracortical injection on the clearance of Aβ plaques in 5xFAD mice. Isotype IgG was injected into the left hemisphere of S1FL as a control, while the right hemisphere of S1FL received anti-PD-L1 treatment in 5xFAD mice. Seven days after anti-PD-L1 injection, we evaluated the size of Aβ plaques in the injection areas (Fig. 6a). We observed a shift towards smaller Aβ plaques in the anti-PD-L1-injected area compared to control IgG-injected area (Fig. 6b). Remarkably, our findings revealed a significant decrease in the size of Aβ plaques compared to control IgG, indicating an augmented clearance of Aβ plaques facilitated by anti-PD-L1 intracortical injection (Fig. 6c).

To confirm that the reduction in Aβ plaque size occurred through microglia-mediated mechanisms, we examined the number of plaque-associated microglia, a subtype of microglial cells that are found near Aβ plaques in brain tissue[38, 39]. We observed an increase in the number of plaque-associated microglia in the cortex with anti-PD-L1 injection (Fig. 6d, e). Quantitative analysis of the co-localization area between CD68 and Aβ, indicating active microglial engulfment, phagocytosis, and clearance of Aβ, was performed in the regions injected with control IgG or anti-PD-L1. Our investigations unveiled a significant increase in the co-localization area of CD68 with Aβ plaques following anti-PD-L1 injection (Fig. 6f, g) which suggests an enhancement in microglial lysosomal activity. Thus, these results suggest that anti-PD-L1 treatment facilitates the efficient clearance of Aβ plaques in the brain, thereby contributing to the therapeutic efficacy in AD.

Discussion

In this study, we investigate the therapeutic potential of targeting the innate immune PD-1/PD-L1 pathway in the brain as a novel strategy for treating AD. We demonstrate that intracortical injection of anti-PD-L1 antibody can rescue both microglial and neuronal function, leading to improved Aβ pathology and restored neuronal calcium activity in the 5xFAD mouse model of AD. This effect is partially mediated through the recruitment of Ly6C^{+} monocytes and macrophages, highlighting the critical role of the crosstalk between glial cells and infiltrated immune cells in the therapeutic process in AD. These results suggest that, in addition to previous research demonstrating that systemic administration of anti-PD-L1 antibody targeting peripheral immune cells could improve AD pathology[2, 3], direct modulation of glial PD-1/PD-L1 signaling within the brain offers a distinct and innovative therapeutic approach for AD.

Our study underscores the complex interplay between immune cells and glial cells in the brain's immune response and homeostatic function in chronically inflamed conditions like AD. In the previous study, increased expression of PD-1 and PD-L1 was reported in the brain tissue and cerebrospinal fluid (CSF) of AD patients, as well as in the brain tissue of AD mouse models[13]. Consistent with these findings, our study observed elevated levels of microglial PD-1 and astrocytic PD-L1 in the cortex and hippocampal areas of the 5xFAD mouse model. While PD-1 and PD-L1 expression were also detected in neurons, their levels remained comparable to those observed in WT mice. Notably, longitudinal analysis of 5xFAD mice revealed that PD-L1 expression levels and astrocytic GFAP expression levels both increase as Aβ plaque deposition progresses, with a strong correlation between them. Importantly, given that GFAP has recently been recognized as a key biomarker in clinical guidelines for AD management[40-42], co-elevation of PD-L1 and GFAP may reflect critical neuroinflammatory processes in AD progression.

Following the direct intracortical injection of anti-PD-L1 antibody into the cortex 5xFAD mice, immunostaining confirmed that the administered antibody bound to astrocytes expressing GFAP, which suggesting GFAP^{+} astrocytes are the main target of brain delivered anti-PD-L1 antibody. Interestingly, peripheral immune cell infiltration was observed only in the 5xFAD brains after anti-PD-L1 treatment, implying that modulating the PD-1/PD-L1 axis between microglia and astrocytes may drive this recruitment. While the mechanism by which anti-PD-L1 binding to astrocytes facilitates immune cell entry remains unclear, it is likely that reshaping astrocyte-microglia interactions leads to the secretion of chemotactic factors[43, 44]. Further research is needed to elucidate the signaling pathways and entry routes involved in this immune cell infiltration.

Peripheral immune cell infiltration in AD treatment presents a complex and double-edged sword, as studies reveal both detrimental and beneficial effects. For instance, studies on CD8^{+} cytotoxic T cells indicate that they infiltrate the AD brain and may contribute to neurodegeneration by directly targeting neurons and promoting neuroinflammation[45, 46]. However, recent research suggests that CD8^{+} T cells, through interactions with microglia, may also play a protective role by limiting disease progression and restraining AD pathology[12]. Monocytes, particularly those differentiating into macrophages, play a dual role by contributing to neuroinflammation as pro-inflammatory cells[47], while also aiding in clearing Aβ plaques through their phagocytic activity, helping to reduce the plaque burden[48]. Treg cells, on the other

hand, primarily exhibit beneficial effects in AD by reducing inflammation and providing neuroprotection, with studies showing that increasing Treg populations in AD models can lower neuroinflammation and AD-related pathological aggregates, thereby maintaining immune balance and supporting brain health[11, 49, 50]. In our study, intracortical injection of anti-PD-L1 facilitates the infiltration of various immune cells, including monocytes, Tregs, and other inflammatory immune cells, into the brain. While this approach holds promise for modulating immune responses in AD, the diverse and sometimes opposing roles of these cells make the situation complex. Unlike acute inflammation-related brain disorders[51, 52], in our AD model, blocking PD-1/PD-L1 signaling appears to rejuvenate microglia from their stalled state without triggering a pathological inflammatory response in our model. Better understanding and refining these immune mechanisms are essential to developing optimized therapeutic strategies that effectively target peripheral immune infiltration without exacerbating AD pathology, underscoring the need for further research.

In various mouse models of AD, studies have reported that the recruitment of peripheral immune cells into the brain is beneficial, achieved through the transient activation of the systemic immune system by blocking PD-1/PD-L1 or depleting Treg cells[2, 3, 53]. This approach has been shown to enhance the clearance of Aβ plaques and improve cognitive function by promoting the infiltration of monocyte-derived macrophages into the brain, which contributes to a neuroprotective environment[2, 3]. Peripheral immune cells may reorganize the brain-immune milieu by releasing various cytokines such as IL-10, which can help attenuate neuroinflammation and support brain homeostasis[54]. Ly6C$^+$ monocytes are a subset of active monocytes that can be recruited to sites of inflammation and subsequently differentiate into macrophages. These macrophages are capable of producing IL-10, an anti-inflammatory cytokine. The capacity of macrophages to produce IL-10 has been demonstrated in various studies, particularly during bacterial infections or inflammatory models, highlighting their role in the resolution of inflammation[55]. We observed IL-10 expression at both 1 and 7 days post-injection of anti-PD-L1 antibody into the brain (Fig. 3h, Extended Data Fig. 8). While IL-10 was not detectable by multiplex chemokine and cytokine analysis on 1 day post-injection, immunofluorescence staining revealed its presence and co-localization alongside infiltrated Ly6C$^+$ monocytes.

Thus, our findings suggest that brain-infiltrated monocytes secrete IL-10, which subsequently binds to its receptor on astrocytes. Astrocytes in AD express IL-10 receptor (IL-10R), and the interaction of IL-10 with IL-10R on astrocytes helps modulate inflammatory responses in the brain[56, 57] (Extended Data Fig. 8). Studies have shown that IL-10 signaling can have neuroprotective effects by reducing the production of pro-inflammatory cytokines and other neurotoxic factors[58]. This interaction stimulates astrocytes to secrete TGF-β, another key anti-inflammatory cytokine[56]. Microglia responds to the increased levels of TGF-β by upregulating P2RY12, a receptor involved in several signaling pathways related to immune response and homeostasis within the brain[34]. Enhancing IL-10 or TGF-β signaling could offer neuroprotective benefits, reducing inflammation and promoting a more balanced immune environment within the brain[34, 56]. Our study clearly showed an increase in monocytic IL-10, astrocytic TGF-β, and microglial P2RY12 following anti-PD-L1 injection. Therefore, these results elucidate a critical immune regulatory pathway involving glial PD-1/PD-L1 axis, monocytes/macrophages, IL-10, TGF-β, and microglial P2RY12. Recent findings have demonstrated that microglia in the AD brain are locked in a stalled state, suggesting that

reprogramming these cells may be a novel therapeutic strategy for AD pathology[12]. Our data, showing elevated levels of PD-1 in microglia and PD-L1 in astrocytes, align with this hypothesis, as these molecules are well-known for suppressing immune responses in peripheral immune cells[48-50].

Furthermore, the roles of microglia have been highlighted in maintaining homeostasis and modulating neuronal activity. Their functions extend beyond traditional immune responses, influencing various aspects of neuronal function and homeostasis. P2RY12 is essential for the maintenance of microglial motility. The proper functioning of P2RY12 signaling allows microglia to continuously monitor neuronal activity. The loss or dysfunction of P2RY12 impairs the chemotactic response of microglia to excessive ATP and ADP released from hyperactive neurons, thereby hindering the regulation of neuronal activity[19]. Following anti-PD-L1 injection, the abnormal hyperactivity in spontaneous neuronal calcium transients observed in 5xFAD mice returned to baseline levels similar to those in WT mice. The restored neuronal homeostasis following anti-PD-L1 injection appears to have repaired the disrupted microglia-neuron crosstalk through astrocytic TGF-β-driven recovery of microglial P2RY12. However, as neurons express TGF-β receptors[59], astrocyte-secreted TGF-β may not only contribute to rescue microglial function to limit neuronal hyperactivity but also directly influence neurons by modulating synaptic transmission, enhancing inhibitory signals, and prevent excitotoxicity through the regulation of glutamatergic activity and intracellular calcium levels, thereby restoring balanced spontaneous neuronal activity[60-62]. Moreover, our findings align with previous research indicating that TGF-β plays a crucial role in promoting Aβ clearance by modulating microglial activity and inflammatory pathways[63].

Our findings demonstrate that anti-PD-L1 treatment not only reduces Aβ plaque size (Fig. 6a-c) but also increases plaque-associated microglia (Fig. 6d, e) and restores homeostatic function in the plaque-associated region, as evidenced by increased P2RY12 levels (Fig. 4a-c). Interestingly, the upregulation of P2RY12 near plaques of similar size (~150 μm^2) suggests that this effect is not merely a consequence of plaque reduction (Extended Data Fig. 7c). Rather, we propose that infiltrating monocytes, following anti-PD-L1 treatment, secrete IL-10, which promotes astrocytic production of TGF-β and restoration of microglial P2RY12. Given that Aβ plaques themselves suppress P2RY12 expression[29, 64], impair microglial function[35], and directly affect neuronal activity[24], it remains critical to distinguish whether these changes arises from the proposed IL-10/TGF-β signaling pathway or are a secondary effect of enhanced plaque clearance. Further studies are warranted to discern whether the observed therapeutic effects following anti-PD-L1 injection are predominantly driven by monocyte-mediated immune modulation with boosted IL-10/TGF-β signaling pathway or by the reduction of Aβ plaque burden.

Current anti-Aβ immunotherapies primarily focus on the clearance of pathological proteins and have shown limited success in fully addressing the complex nature of the disease. These therapies often fail to effectively modulate the intricate peripheral-central immune crosstalk that is crucial for maintaining brain immune system balance. To advance beyond these limitations, there is a growing need for next-generation disease-modifying drugs that not only target Aβ clearance but also rebalance the brain's immune system through novel mechanisms. Targeting immune checkpoints, such as PD-1/PD-L1, restore microglial homeostasis and improve neuronal function could be a promising therapeutic strategy for AD. Combining this

approach with innovative BBB transport technologies could further enhance the delivery and efficacy of these treatments. Moreover, a combinatorial tandem therapy involving anti-Aβ agents followed by PD-1/PD-L1 immune checkpoint blockade can present a promising strategy. Such an approach could sequentially target Aβ pathology while subsequently modulating the neuroinflammatory environment, potentially leading to more comprehensive therapeutic outcomes. Further preclinical and clinical studies are needed to explore these possibilities and to validate the therapeutic efficacy and safety of immune checkpoint blockade in AD.

438 Methods

439 **Animal models**

440 All experimental procedures received approval from the Institutional Animal Care and Use
441 Committee (IACUC) of Sungkyunkwan University (SKKU). The experiments were carried out
442 following the guidelines established by the Guide for the Care and Use of Laboratory Animals,
443 in compliance with the Animal Protection Law and the Laboratory Animal Act, as regulated by
444 the Korea Animal and Plant Quarantine Agency and the Korea Ministry of Food and Drug
445 Safety. The mouse lines used in the study include: C57BL/6J mice, B6.Cg-
446 Tg(APPSwFlLon,PSEN1*M146L*L286V)6799Vas/Mmjax (5xFAD)[65] and B6.129P2(Cg)-
447 *Cx3cr1*^{tm1Litt}/J (CX3CR1$^{GFP/GFP}$)[66] from the Jackson Laboratory. 6-to-10-month-old 5xFAD
448 mice and age-matched WT littermates were used in this study.

449

450 **Intracortical injection of anti-PD-L1 antibody**

451 Mice were initially anesthetized using 3% isoflurane for induction and maintained under 1%-
452 1.5% isoflurane throughout the surgery using an isoflurane vaporizer (VetEquip). They were
453 positioned in a stereotaxic frame on a temperature-controlled heating pad (FHC) set at 37°C to
454 maintain body temperature. The head skin of mouse was sanitized with an alcohol swab
455 (isopropyl alcohol 70%, BD) and then incised using surgical scissors. A small craniotomy was
456 performed over the primary somatosensory cortex of the forelimb region (S1FL) on both sides.
457 The left hemisphere was injected with a control isotype antibody, while the right hemisphere
458 was injected with an anti-PD-L1 antibody. To examine the immune cell population, we injected
459 five sites in each hemisphere, totaling ten sites, to ensure sufficient cell numbers for FACS
460 sorting. For *in vivo* two-photon experiments, the injection was administered only in the right
461 S1FL at a 40-degree angle to avoid major blood vessels and minimize potential tissue damage
462 above the injection site during an acute craniotomy for imaging.

463 Mouse PD-L1-blocking antibody (anti-PD-L1; cat# BE0101, rat IgG2b, κ, clone 10F.9G2, Bio
464 X cell, 1 μg in 1 μL) was delivered using a 10 μl Hamilton syringe equipped with a fine glass
465 pipette at a rate of 80 nl/min, connected to a syringe pump (Harvard Apparatus). Isotype control
466 IgG antibody (anti-keyhole limpet hemocyanin; cat# BE0090, rat IgG2b, κ, clone LTF-2, Bio
467 X cell, 1 μg in 1 μL) was injected following the same procedure. The glass pipette remained in
468 place for 5 minutes post-injection to minimize backflow. Subsequently, the drilled holes were
469 sealed with bio-compatible surgical elastomer Kwik-Sil (WPI), the skin was sutured using
470 surgical sutures (B. Braun Surgical), and veterinary adhesive (Vetbond, Fisher Scientific) was
471 applied. The animals were then returned to their home cages. After injection of antibody, mice
472 were allowed to recover with the application of antibiotics (Baytril; 5 mg/kg, s.c. injection) and
473 analgesics (Meloxicam; 1 mg/kg, s.c. injection) and were closely monitored for any signs of
474 distress.

475

476 **Multiparameter flow cytometry analysis and cell sorting**

477 Mice were deeply anesthetized 2.5% avertin (400 mg/kg, i.p., cat# 240486, Sigma) and
478 perfused with 0.1 M phosphate buffered saline (PBS). After the brain were extracted, brain

tissue were mechanically minced and incubated in dissociation buffer for 30 min at 37 °C, containing 0.1 mg/mL DNase I (Roche), 1 mg/mL Collagenase type IV (Gibco), 2% FBS in DMEM Medium. Digested brain tissue was gently mashed through a 70 μm strainer and centrifuged at 750 g for 5 min at 4 °C in a swinging bucket rotor. Pellets were resuspended with 35% Percoll in PBS (Cytiva) and centrifuged in 1120 g for 20 min at room temperature (RT) to remove myelin debris. Pellets were resuspended in DMEM with 10% FBS for further analysis.

For the flow cytometry analysis, isolated cells were surface-stained with following antibodies: CD45-BUV395 (1:200 dilution, cat# 564279, clone 30-F11, BD), CD8-BUV805 (1:200 dilution, cat# 612898, clone 53-6.7, BD), CD62L-BUV737 (1:200 dilution, cat# 612833, clone MEL-14, BD), CD44-BUV615 (1:200 dilution, cat# 751414, clone IM7, BD), F4/80-BUV661 (1:200 dilution, cat# 750643, clone T45-2342, BD), MHCII-BUV496 (1:200 dilution, cat# 750281, clone M5/114.15.2, BD), NK1.1-BUV563 (1:200 dilution, cat# 741233, clone PK136, BD), TCRγδ-BV605 (1:200 dilution, cat# 107502, clone UC7-13D5, BioLegend), TCRβ-BV650 (1:200 dilution, cat# 109207, clone H57-597, BioLegend), Ly6C-BV785 (1:200 dilution, cat# 128041, clone HK1.4, BioLegend), CD127-PE-Cy5 (1:200 dilution, cat# 135015, clone A7R34, BioLegend), CD11b-PerCP-Cy5.5 (1:200 dilution, cat# 101227, clone M!/70, BioLegend), CD11c-PE-Cy7 (1:200 dilution, cat# 117317, clone N418, BioLegend), CD19-APC-R700 (1:200 dilution, cat# 565473, clone 1D3, BD), CD4-APC-Cy7 (1:200 dilution, cat# 100413, clone GK1.5, BioLegend), C-kit-PerCP (1:200 dilution, cat# 105801, clone 2B8, BioLegend), FcεRIα-AF647 (1:200 dilution, cat# 134309, clone MAR-1, BioLegend). LIVE/DEAD™ Fixable Aqua (Thermo Fisher Scientific, USA) was added to staining solution to discriminate dead cells. After incubation at 4 °C for 30 min, the cells were fixed and permeabilized with eBioscience™ Foxp3 / Transcription Factor Staining Buffer (Invitrogen, USA) and were stained with following antibodies at RT for 40 min: FOXP3-AF488 (1:100 dilution, cat# 53-5773-82, clone FJK-16s, Invitrogen), HELIOS-PB (1:100 dilution, cat# 137210, clone 22F6, BioLegend), RORγt-PE (1:100 dilution, cat# 12-6981-82, clone B2D, Invitrogen). After staining, cells were washed with PBS and data acquisition was performed by Sony ID7000 (Sony).

For the cell sorting, isolated cells were stained with the following antibodies: CD11b-FITC (1:200 dilution, cat# 101205, clone M1/70, BioLegend), ACSA-2-PE (1:200 dilution, cat# 130-123-284, clone IH3-18A3, Miltenyi Biotec), CD45-APC-Cy7 (1:200 dilution, cat# 103115, clone 30-F11, BioLegend). After staining, cells were washed with PBS and cell pellets were resuspended in DMEM with 10% FBS. DAPI was added to distinguish dead cells. Microglia and astrocytes were sorted on the Sony MA900 cell sorter (Sony).

The gating strategies for flow cytometric analysis and cell sorting are described in Extended Data Figure 3 and Extended Data Figure 4. Flow cytometric data were analyzed in FlowJo v10.9.0 (BD). UMAP algorithm for dimensionality reduction was applied using the UMAP plugin (v3.1) available on FlowJo.

RNA isolation and reverse transcription-quantitative PCR analysis

For quantification of mRNA, mRNA was extracted from sorted cells using RNeasy Micro Kit (Qiagen), and PrimeScript™ II 1st strand cDNA Synthesis Kit (Takara) was used for reverse

522 transcription. PowerUp™ SYBR® Green PCR Master Mix (Thermo Fisher) and QuantStudio3
523 (Applied Biosystems) was used for quantitative PCR analysis with following primers targeting
524 *Tgfb1* (F: 5'- CTCCCGTGGCTTCTAGTGC-3', R: 5'- GCCTTAGTTTGGACAGGATCTG-
525 3').

526

527 **Multiplex chemokine and cytokine analysis**

528 For multiplex chemokine and cytokine analysis, anti-PD-L1 and control IgG injected cortical
529 region was dissected, and brain lysate was prepared with Cell lysis buffer (Cell signaling) by
530 homogenization and sonication. Chemokine and cytokine in plasma were measured using
531 LEGENDplex™ Mouse Proinflammatory Chemokine Panel (cat# 740007, BioLegend) for
532 CCL5 ,CCL20, CCL11, CCL17, CXCL1, CCL2, CXCL9, CXCL10, CCL3, CCL4, CXCL13,
533 CXCL5, CCL22, Mouse Proinflammatory Chemokine Panel 2 (cat# 741068, BioLegend) for
534 CCL24, CCL8, CXCL11, CX3CL1, CCL7, XCL1, CXCL2, CCL9, Mouse Th Cytokine Panel
535 (cat# 741044, BioLegend) for IFN-γ, IL-5, TNF-α, IL-2, IL-6, IL-4, IL-10, IL-9, IL-17A, IL17F,
536 IL-22, IL-13 and Mouse Cytokine Panel 2 (cat# 740134, BioLegend) for IL-1α, IL-1β, IL-3,
537 IL-7, IL-11, IL-12p40, IL-12p70, IL-23, IL-27, IL-33, IFN-β, GM-CSF, TSLP. For each sample,
538 more than 300 beads were recorded using BD FACSCelesta (BD) and analyzed using the Data
539 Analysis Software Suite for LEGENDplex, a free cloud-based program
540 (https://legendplex.qognit.com/).

541

542 **Immunostaining and Histological Analysis**

543 Mice were anesthetized with 2.5% avertin (400 mg/kg, i.p.) and perfused with 0.1 M PBS
544 followed by 4% paraformaldehyde (PFA) using a peristaltic pump (P-1500, Harvard apparatus)
545 after receiving intracortical injection on either day 1 or day 7. The perfused brains were placed
546 in 4% PFA for 24 hours at 4 °C, followed by immersion in 30% sucrose in PBS for 3 days.
547 40μm-thick coronal brain tissue sections were permeabilized with 0.5% Triton X-100 in PBS
548 for 10 min at RT, blocked with 10% donkey serum, and then incubated with the primary
549 antibody overnight at 4 °C. The following primary antibodies were used: rabbit anti-PD-1
550 (1:300 dilution, cat# PRS4065, Sigma), rat anti-PD-L1 (1:500 dilution, cat# BE0101, Bio X
551 Cell), rabbit anti-Iba1 (1:300 dilution, cat# 234-004, Wako), goat anti-Iba1 (1:300 dilution, cat#
552 ab5076, Abcam), mouse anti-GFAP (1:400 dilution, cat# MAB360, Millipore), goat anti-GFAP
553 (1:400 dilution, cat# ab53554, Abcam), mouse anti-NeuN (1:800 dilution, cat# ab104224,
554 Abcam), rabbit anti-NeuN (1:800 dilution, cat# 234009, Abcam), rat anti-IL-10 (1:100 dilution,
555 cat# ab189392, Abcam), rat anti-CD210 (IL-10 receptor) (1:500 dilution, cat# 112706,
556 BioLegend), rabbit anti-P2RY12 (1:1000 dilution, cat# ab300140, Abcam), rabbit anti-GFP
557 (1:800 dilution, cat# A-11122, Invitrogen), mouse anti-β-Amyloid 1-16 (6E10) (1:1000
558 dilution, cat# 803014, BioLegend), rat anti-CD68 (1:200 dilution, cat# MCA1957, Bio-Rad).
559 The following day, sections were washed in PBS and then incubated in secondary antibodies
560 for 2 h at RT. The following secondary antibodies were applied respectively; anti-rat IgG
561 Alexa488 (donkey, 1:400 dilution, cat# A21208, donkey, Invitrogen), anti-goat IgG Alexa555
562 (donkey, 1:400 dilution, cat# A21432, Invitrogen), anti-goat IgG Alexa633 (donkey, 1:400
563 dilution, cat# A21082, Invitrogen), anti-mouse IgG Alexa488 (donkey, 1:400 dilution, cat#

A21202, Invitrogen), anti-mouse IgG Alexa568 (donkey, 1:400 dilution, cat# A10037, Invitrogen), anti-rabbit IgG Alexa488 (donkey, 1:400 dilution, cat# A21206, Invitrogen), anti-rabbit IgG Alexa568 (donkey, 1:400 dilution, cat# A10042, Invitrogen), anti-rabbit IgG Alexa647 (donkey, 1:400 dilution, cat# A31573, Invitrogen). For Thioflavin S staining (ThioS, diluted in 50% ethanol, cat# T1892, Sigma), brain sections were incubated in 0.5% ThioS for 10 min at RT. Nuclear counterstaining was performed with 100 ng/ml DAPI solution (1:10,000 dilution, cat# D9542, Sigma) in PBS for 10 min.

Confocal microscopy (TCS SP8, Leica Microsystems) was used for fluorescence imaging, with both Fiji[67] and IMARIS (Bitplane) software employed for quantitative analysis of staining intensity and cellular localization. To analyze the cell-specific expression of PD-1 and PD-L1, fluorescence images obtained using anti-Iba1, anti-GFAP, and anti-NeuN primary antibodies were converted to binary, and the immunoreactivity of PD-1 and PD-L1 within the ROIs was calculated. Assessment of microglial phagocytosis and Aβ clearance was conducted with colocalization of microglia-specific lysosome marker (CD68) and Aβ (6E10) on confocal optical sections using IMARIS with its module[68]. The brightest approximately 2% of pixels in each channel were examined to determine the threshold for colocalization in an unbiased manner, eliminating problems caused by inevitable imaging variations.

Cranial window surgery in mice

Initially, mice were anesthetized using 3% isoflurane for induction and maintained under 1%-1.5% isoflurane throughout the surgery. Body temperature was carefully maintained at 37°C using a temperature-controlled heating pad (FHC). A cranial window was surgically created over the cortex to facilitate imaging, with the dura mater left intact. The exposed cortex was hydrated with HEPES-buffered saline (135 mM NaCl, 5 mM KCl, 10 mM HEPES, 10 mM glucose, 2 mM $CaCl_2$, 2mM $MgSO_4$) or HEPES-buffered saline-soaked GelFoam sponges (MS0005, Ethicon). After confirming the absence of microbleeding, a glass coverslip was placed over the exposed cortex (4 mm diameter, Deckglaser). To stabilize the cranial window and prevent animal head movements during imaging, a custom-made metal holding frame was affixed to the skull. This frame also allowed for the adjustment of the cranial window angle to ensure it remained perpendicular to the microscope objective axis. Throughout the experiments, the physiological parameters such as heart rate, SpO2, and respiration rate were continuously monitored using a paw sensor (PhysioSuite, Kent Scientific) to ensure they remained within normal ranges. At the conclusion of all experimental procedures, the mice were euthanized by CO_2 inhalation in a closed chamber.

In Vivo Two-Photon Imaging

In vivo two-photon imaging was performed to visualize microglial dynamics and spontaneous neuronal activity in live mice. A two-photon microscope (TCS SP8 MP, Leica Microsystems) equipped with a Ti:sapphire laser (Chameleon Vison II, Coherent) was used for brain imaging. Imaging was performed using a 25× water-immersion objective lens (NA 0.95, Leica Microsystems) and a green bandpass emission filter set at 520 ± 50 nm. Isoflurane anesthesia can affect the homeostatic function of microglia and neuronal activity[69]. To minimize these

effects, the mice were kept under light isoflurane anesthesia, with the concentration carefully maintained at a low level (~0.8%) throughout the imaging process, as done in previous studies[24, 26, 27, 70, 71].

For *in vivo* two-photon imaging of microglia, we crossbred 5xFAD mice with CX3CR1-GFP mice, where microglia are genetically modified to express green fluorescent protein (GFP) under the control of the CX3CR1 promoter. This crossbreeding produced offspring with fluorescence specifically in microglia, enabling targeted imaging and analysis of microglial dynamics within the 5xFAD model. Imaging was conducted at wavelengths tuned to 920 nm, focusing on regions deeper than 250 μm in the cortex, which had been injected with either anti-PD-L1 or isotype control antibodies. For laser-induced injury, the laser was focused at ~50 mW for 60 seconds. Microglial responses were calculated using the formula: $(I_f(t) - I_f(0)) / I_s(t)$, where I_f represents the intensity at the focus (with a diameter of 50 μm) and I_s represents the intensity of the surrounding area, forming a donut-like shape due to the subtraction of the focus[36].

For *in vivo* two-photon imaging of neurons, AAV9-CamKII-GCaMP6f virus (Plasmid #100834, titer: 3.1 x 10^{13} GC/ml) was co-delivered with either anti-PD-L1 or isotype control antibodies to visualize excitatory neuronal calcium activity. Spontaneous Ca^{2+} fluorescence signals from cortical layer 2/3 were recorded at a frequency of ~15 Hz. Imaging was conducted across multiple regions per mouse, with each region recorded for at least 2 minutes. Cell ROIs were drawn around individual neuronal somata, and then relative GCaMP6f fluorescence changes over time were generated for each ROI. Neurons were classified based on their activity rates, with hyperactive neurons defined as those exhibiting ≥4 transients per minute[24].

Statistical analysis

Statistical analyses were conducted using GraphPad Prism 9.5.1 (GraphPad Software, USA) or IBM SPSS Statistics 19 (SPSS Inc., USA). Mann-Whitney U-tests were employed for comparisons between two groups, with Wilcoxon signed-rank tests used for paired data. For comparisons involving more than three groups, Dunn's multiple comparisons test was utilized, with Bonferroni *post hoc* procedure applied for pairwise comparisons. Spearman's correlation coefficient was applied to assess the relationship between the two variables. Ordinary least squares (OLS) regression was used to fit a linear model to the data points. Statistical significance is indicated within the figures by * for $p < 0.05$, ** for $p < 0.01$, *** for $p < 0.001$, and **** for $p < 0.0001$.

Acknowledgements

We would like to thank Hyouna Yoo, Euna Lee, Jae Hoon Jeong, Hyojung Kim, and Bok-Man Kang of IMNEWRUN Inc. for their helpful discussions and comments on the manuscript. We also thank Gyeong Eon Kim for proofreading the manuscript. This research was supported by a grant of the Korea Dementia Research Project through the Korea Dementia Research Center (KDRC), funded by the Ministry of Health & Welfare and Ministry of Science and ICT, Republic of Korea (No. RS-2024-00344426); the Institute for Basic Science (No. IBS-R015-

D1); the National Research Foundation of Korea (NRF) funded by the Korea government (MSIT) (No. 2017R1A6A1A03015642, 2023R1A2C1004318, RS-2023-00302458, 2022M3A9I2017587, 2022M3E5E8018388); Institute of Information & communications Technology Planning & Evaluation (IITP) grant funded by the Korea government (MSIT) (No. 2020-0-00261); the Fourth Stage of Brain Korea 21 Project in Department of Intelligent Precision Healthcare, Sungkyunkwan University (SKKU) (No. RS-2022-0608-000); a grant of the Korea Health Technology R&D Project through the Korea Health Industry Development Institute (KHIDI), funded by the Ministry of Health & Welfare, Republic of Korea (RS-2024-00438443). This research was also supported by KIST-SKKU Brain Research Center and IMNEWRUN Inc.

Author contribution

T.P., H.-J.K., and M.S. conceptualized the study; T.P., and M.S. designed the experiments; L.C., and H.-K.K. performed cellular and molecular immunoassays; T.P. and S.B. performed immunofluorescence staining experiments; T.P., S.W.C., and S.L. performed the stereotaxic injections and histological analysis; T.P. performed *in vivo* two-photon imaging experiments and analyzed data; T.P., L.C., H.-K.K. and M.S. wrote the manuscript; C.C., Y.H.K., J.L., and H.-J.K., revised the manuscript; all authors edited and reviewed the final manuscript.

Corresponding authors

Correspondence to Ho-Keun Kwon or Minah Suh

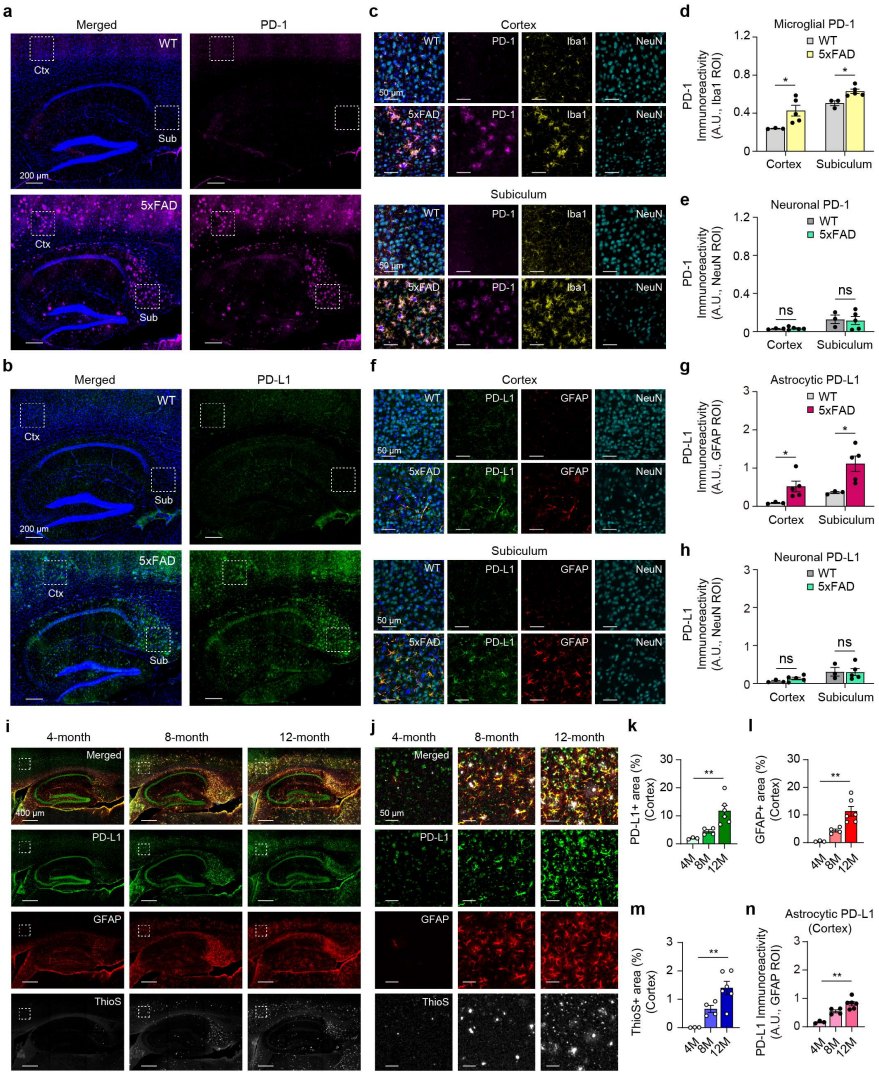

Figure 1. Upregulated expression of microglial PD-1 and astrocytic PD-L1 is found in 8-month-old 5xFAD mice.

a, Representative confocal microscopy images of PD-1 immunoreactivity (magenta) stained with DAPI (blue) in control brains and 5xFAD mouse brains. Ctx indicates cortex. Sub indicates subiculum. **b**, Representative confocal microscopy images of PD-L1 immunoreactivity (green) stained with DAPI (blue) in control brains and 5xFAD mouse brains. **c**, Magnification images of white dashed box in **a**. Colocalization are shown in merged images. Brain slices were stained with DAPI (blue), PD-1 (magenta), microglial marker Iba1 (yellow), and neuronal marker NeuN (cyan). **d**, Quantification showing microglial PD-1 expression in the 5xFAD brain (WT; $n = 3$ mice, 5xFAD; $n = 5$ mice, Mann–Whitney U test; cortex; $*p = 0.025$, subiculum; $*p = 0.025$, mean ± s.e.m.). **e**, Quantification showing neuronal PD-1 expression in the 5xFAD brain (WT; $n = 3$ mice, 5xFAD; $n = 5$ mice, Mann–Whitney U test; cortex; $p = 0.881$, subiculum; $p = 0.655$, mean ± s.e.m., ns, not significant). **f**, Magnification images of white dashed box in **b**. Colocalization are shown in merged image. Brain slices were stained with DAPI (blue), PD-L1 (green), astrocytic marker GFAP (red) and NeuN (cyan). **g**, Quantification showing astrocytic PD-L1 expression in the 5xFAD brain (WT; $n = 3$ mice, 5xFAD; $n = 5$ mice, Mann–Whitney U test; cortex; $*p = 0.025$, subiculum; $*p = 0.025$, mean ± s.e.m.). **h**, Quantification showing neuronal PD-L1 expression in the 5xFAD brain (WT; $n = 3$ mice, 5xFAD; $n = 5$ mice, Mann–Whitney U test; cortex; $p = 0.297$, subiculum; $p = 0.881$, mean ± s.e.m., ns, not significant). **i**, Representative images showing age-dependent changes in PD-L1 (green), GFAP (red), and Thioflavin S (ThioS) (gray) in 5xFAD mouse brains at different disease stages. **j**, Magnification images of white dashed box in **i** (cortex). **k-m**, Quantification of PD-L1, GFAP, and Aβ (ThioS) expression levels across time points (4M = 4-month-old; $n = 3$ mice, 8M = 8-month-old; $n = 4$ mice, 12M = 12-month-old; $n = 6$ mice, Kruskal-Wallis test with Dunn's post-hoc comparisons test; PD-L1 4M vs 8M; $p = 0.7179$, PD-L1 4M vs 12M; $**p = 0.0061$, PD-L1 8M vs 12M; $p = 0.1401$; GFAP 4M vs 8M; $p = 0.7179$, GFAP 4M vs 12M; $**p = 0.0061$, GFAP 8M vs 12M; $p = 0.1401$; ThioS 4M vs 8M; $p = 0.5361$, ThioS 4M vs 12M; $**p = 0.0091$, ThioS 8M vs 12M; $p = 0.2923$, mean ± s.e.m.). **n**, Quantification showing age-dependent astrocytic PD-L1 expression in the 5xFAD brain (4M; $n = 3$ mice, 8M; $n = 4$ mice, 12M; $n = 6$ mice, Kruskal-Wallis test with Dunn's post-hoc comparisons test; 4M vs 8M; $p = 0.5361$, 4M vs 12M; $**p = 0.0091$, 8M vs 12M; $p = 0.2923$, mean ± s.e.m.).

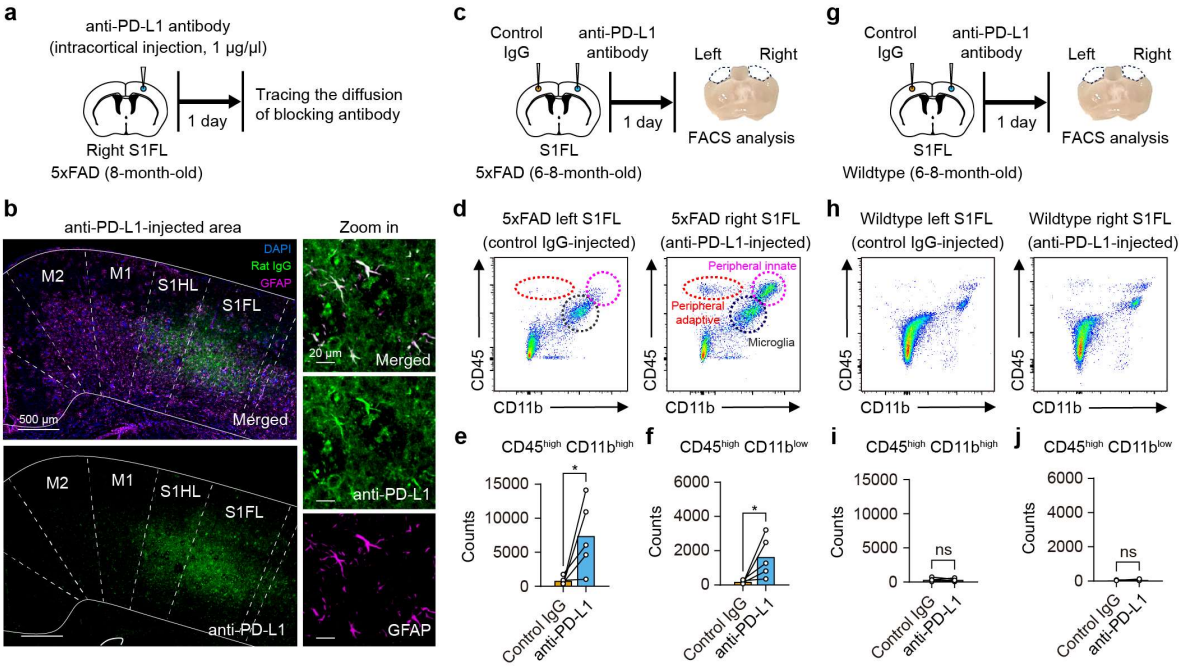

Figure 2. Direct intracortical injection of anti-PD-L1 antibody binds to astrocytes and peripheral immune cells infiltrates 1 day post injection.

a, Experimental scheme of intracortical injection of anti-PD-L1 antibody in 8-month-old 5xFAD mice. **b**, Representative immunofluorescence images showing astrocytes and injected materials. Immunostaining for GFAP (magenta) and DAPI (blue), tracking the distribution of the anti-PD-L1 antibody (green) within the somatosensory cortex forelimb region (S1FL; 0 mm AP, ±2.3 mm ML, −0.5 mm DV) of 8-month-old 5xFAD mice, 1 day after single intracortical injection (left, 1 μg/μl). The magnified images (right), displaying the anti-PD-L1 antibody (green) and GFAP (magenta). **c**, Experimental scheme of flow cytometry analysis of 5xFAD brain tissues by CD11b and CD45 staining in S1FL at 1 day after single intracortical injection. **d**, Representative flow cytometry plots showing peripheral immune cells isolated from the hemispheres of control IgG-injected area (left hemisphere) and anti-PD-L1-injected area (right hemisphere). **e**, Quantification of innate immune cell infiltration into the brain (n = 5 mice, Wilcoxon signed-rank test; *p = 0.043). **f**, Quantification of adaptive immune cell infiltration into the brain (n = 5 mice; Wilcoxon signed-rank test; *p = 0.043). **g**, Experimental scheme of flow cytometry analysis of WT brain tissues by CD11b and CD45 staining in S1FL at 1 day after single intracortical injection. **h**, Representative flow cytometry plots showing peripheral immune cells isolated from the hemispheres of control IgG-injected area (left hemisphere) and anti-PD-L1-injected area (right hemisphere). **i**, Quantification of innate immune cell infiltration into the brain (n = 5 mice; Wilcoxon signed-rank test; p = 0.893, ns, not significant). **j**, Quantification of adaptive immune cell infiltration into the brain (n = 5 mice; Wilcoxon signed-rank test; p = 1.000, ns, not significant).

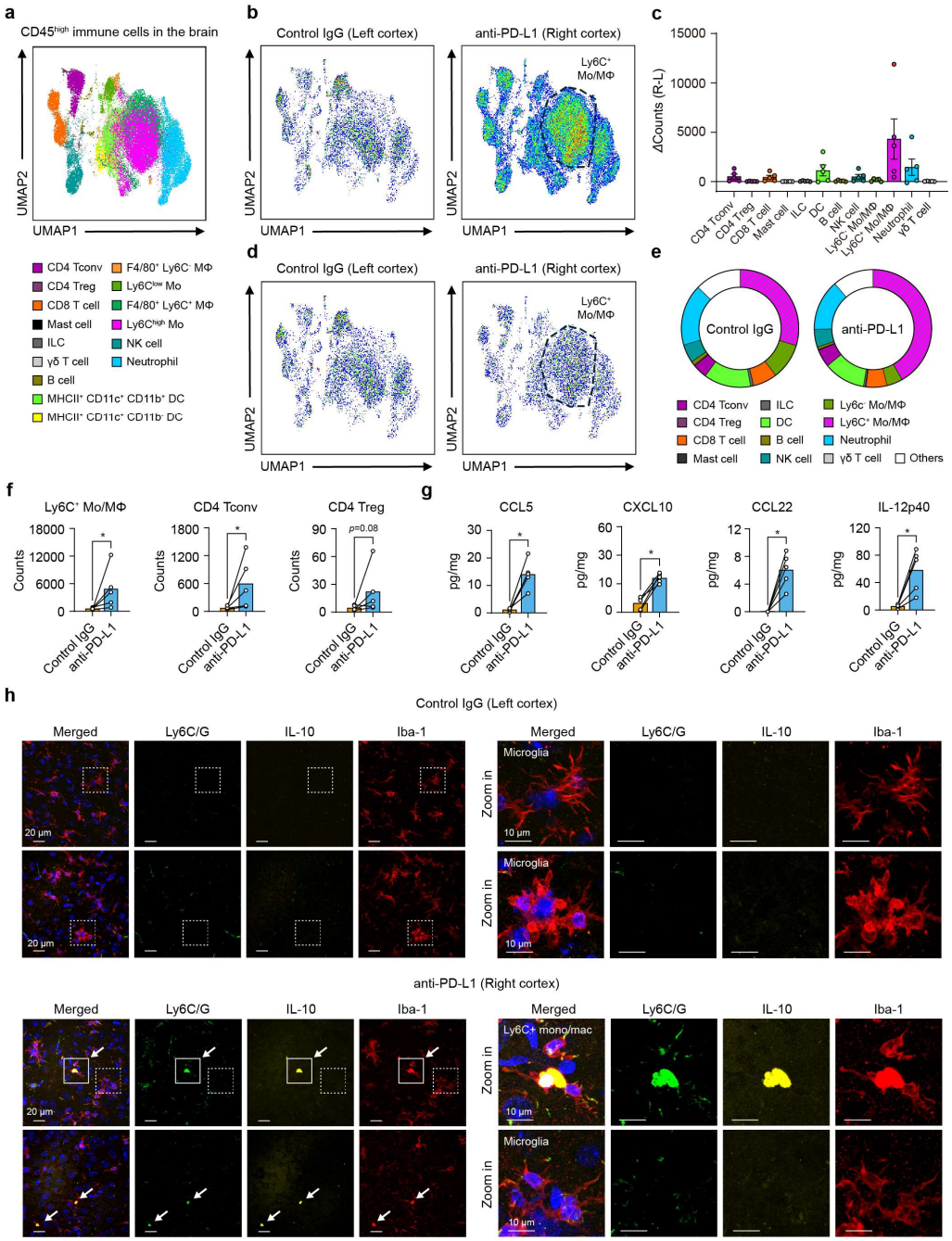

Figure 3. Characterization of infiltrated immune cell populations and chemokine/cytokine levels in the cortex of 5xFAD mice following intracortical injection of anti-PD-L1.

a, UMAP demonstrating cell types of infiltrated immune cells from the cortex of 8-month-old 5xFAD mice injected intracortically with control IgG and anti-PD-L1. **b**, Cell count plots. **c**, A graph showing the number of cells for each cell type, obtained by subtracting the number of cells in the control IgG injection group from the number of cells in the anti-PD-L1 injection group (n = 5 mice, mean ± s.e.m.). **d**,**e**, Cell proportion plots from single-cell analysis, down-sampled to 10,000 cells from the original dataset. **f**, Graphs showing number of infiltrated immune cells in the control IgG- and anti-PD-L1-injected cortex region (n = 5 mice, Wilcoxon signed-rank test; Ly6C$^+$ Mo/MΦ; *p = 0.043, CD4 Tconv; *p = 0.043, CD4 Treg; p = 0.080, ns, not significant). **g**, Graphs showing levels of cytokines and chemokines in the control IgG- and anti-PD-L1-injected cortex region (n = 5 mice, Wilcoxon signed-rank test; CCL5; *p = 0.043, CXCL10; *p = 0.043, CCL22; *p = 0.043, IL-12p40; *p = 0.043). **h**, Representative confocal images, showing colocalization of Ly6C$^+$ (green) Iba1$^+$ (red) cells, and IL-10 (yellow) in the control IgG-injected cortex region (top) and anti-PD-L1-injected cortex region (bottom) of 5xFAD mice (line box; Ly6C/G$^+$ monocytes and macrophages, dashed box; microglia, arrow; IL-10$^+$ Ly6C/G$^+$ monocytes and macrophages). The magnified images (right), displaying microglia or infiltrated immune cells.

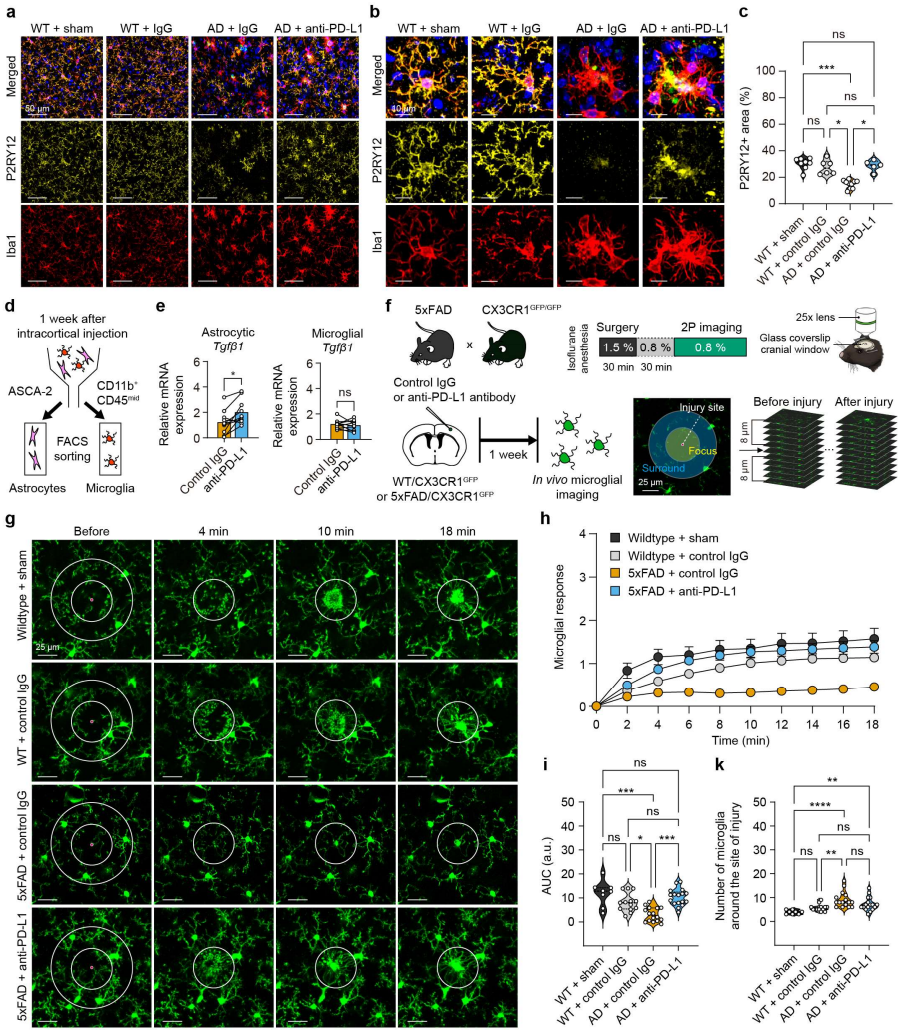

Figure 4. Blockade of PD-1/PD-L1 signaling rescues P2RY12 expression and increases microglial process convergence in response to local brain injury in 5xFAD mice.

a, Representative images of P2RY12^{+} (yellow) and Iba1^{+} (red) microglia at 7 days after single intracortical injection. **b**, Representative images of plaque-associated microglia after single intracortical injection. **c**, Quantitation of P2RY12-positive area (WT + sham; n = 8 mice, WT + control IgG; n = 6 mice, 5xFAD + control IgG; n = 10 mice, 5xFAD + anti-PD-L1; n = 5 mice, Kruskal-Wallis test with Dunn's post-hoc comparisons test; WT + sham vs. WT + control IgG; p = 1.000, WT + sham vs. AD + control IgG; ***p = 0.0003, WT + sham vs. AD + anti-PD-L1; p = 1.000, WT + control IgG vs. AD + control IgG; *p = 0.0211, WT + control IgG vs. AD + anti-PD-L1; p = 1.000, AD + control IgG vs. AD + anti-PD-L1; *p = 0.0198, ns, not significant). **d**, Experimental scheme of FACS sorting of astrocytes and microglia at 7 days after single intracortical injection of control IgG and anti-PD-L1 in 8-month-old 5xFAD mice. **e**, Relative astrocytic and microglial mRNA levels of *Tgfβ1* (n = 10 mice; Wilcoxon signed-rank test; astrocytes; *p = 0.017, microglia; p = 0.575, ns, not significant). **f**, Experimental scheme of *in vivo* microglial time-lapse imaging with focal laser injury at 7 days after single intracortical injection of antibody in 5xFAD/CX3CR1^{GFP} mice by crossing 5xFAD with CX3CR1$^{GFP/GFP}$ mice. **g**, Representative time-lapse imaging of laser injury targeted microglial process convergence. **h**, Time course of microglial process kinetics towards a laser-induced lesion (WT + sham; n = 8, WT + control IgG; n = 13, 5xFAD + control IgG; n = 16, 5xFAD + anti-PD-L1; n = 17). Microglial responses = $I_f(t)-I_f(0)/I_s(t)$; I_f indicates intensity of focus; I_s indicates intensity of surround (mean ± s.e.m.). **i**, Area under the curve (AUC) of the accumulated graphs in **h** (WT + sham; n = 8, WT + control IgG; n = 13, 5xFAD + control IgG; n = 16, 5xFAD + anti-PD-L1; n = 17, Kruskal-Wallis test with Dunn's post-hoc comparisons test; WT + sham vs. WT + control IgG; p = 0.8985, WT + sham vs. AD + control IgG; ***p = 0.0005, WT + sham vs. AD + anti-PD-L1; p = 1.000, WT + control IgG vs. AD + control IgG; *p = 0.0288, WT + control IgG vs. AD + anti-PD-L1; p = 1.000, AD + control IgG vs. AD + anti-PD-L1; ***p = 0.0001, ns, not significant). **j**, Number of microglia around the site of focal injury within 100 µm (WT + sham; n = 8, WT + control IgG; n = 13, 5xFAD + control IgG; n = 16, 5xFAD + anti-PD-L1; n = 17, Kruskal-Wallis test with Dunn's post-hoc comparisons test; WT + sham vs. WT + control IgG; p = 0.2956, WT + sham vs. AD + control IgG; ****p < 0.0001, WT + sham vs. AD + anti-PD-L1; **p = 0.0039, WT + control IgG vs. AD + control IgG; **p = 0.0096, WT + control IgG vs. AD + anti-PD-L1; p = 0.7014, AD + control IgG vs. AD + anti-PD-L1; p = 0.5063, ns, not significant).

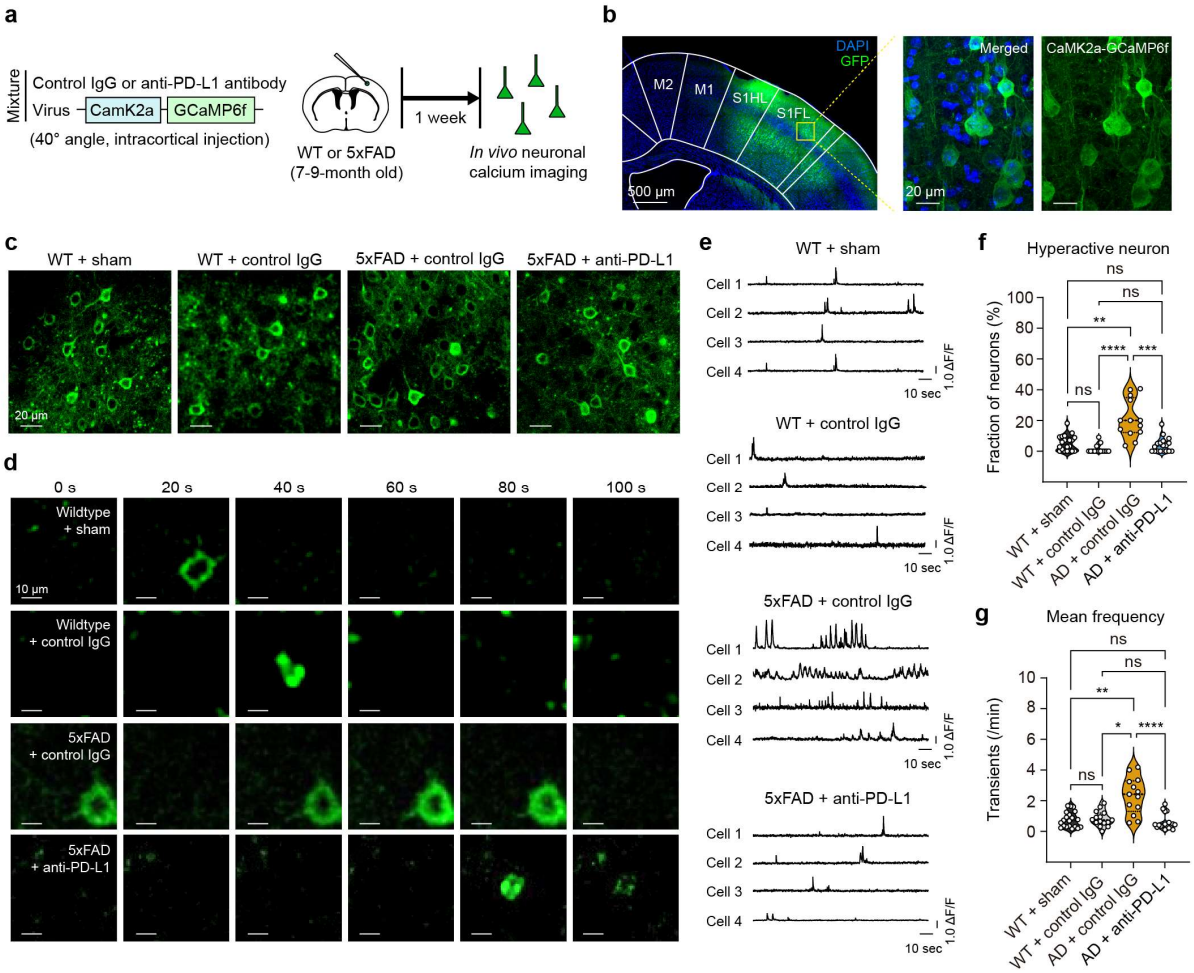

Figure 5. Blockade of PD-1/PD-L1 signaling rescues neuronal activity in 5xFAD mice.

a, Experimental scheme of *in vivo* neuronal calcium imaging intracortical injection of the mixture of antibody and CamK2a-GCaMP6f virus in S1FL at 7 days after single intracortical injection. **b**, Confocal images displaying the expression of the injected virus (green: CamK2a-GCaMP6f, blue: DAPI) in the S1FL. **c**, Representative *in vivo* two-photon fluorescence images of GCaMP6f-expressing cortical neurons from layer 2/3 of control IgG or anti-PD-L1 antibody injected 7-9-month-old 5xFAD mice and age-matched WT mice. **d**, Example fluorescence images of spontaneous calcium transients of a single excitatory neuron in each group. **e**, Representative calcium fluorescent traces of neurons. **f**, Fractions of hyperactive neurons in sham or control IgG-injected WT mice and control IgG- or anti-PD-L1-injected AD mice (WT + sham; $n = 20$, WT + control IgG; $n = 15$, 5xFAD + control IgG; $n = 13$, 5xFAD + anti-PD-L1; $n = 18$, Kruskal-Wallis test with Dunn's post-hoc comparisons test; WT + sham vs. WT + control IgG; $p = 0.1790$, WT + sham vs. AD + control IgG; $^{**}p = 0.0039$, WT + sham vs. AD + anti-PD-L1; $p = 1.000$, WT + control IgG vs. AD + control IgG; $^{****}p < 0.0001$, WT + control IgG vs. AD + anti-PD-L1; $p = 1.000$, AD + control IgG vs. AD + anti-PD-L1; $^{***}p = 0.0002$, ns, not significant). **g**, Mean frequency of neuronal calcium transients (WT + sham; $n = 20$, WT + control IgG; $n = 15$, 5xFAD + control IgG; $n = 13$, 5xFAD + anti-PD-L1; $n = 18$, Kruskal-Wallis test with Dunn's post-hoc comparisons test; WT + sham vs. WT + control IgG; $p = 1.0000$, WT + sham vs. AD + control IgG; $^{**}p = 0.0015$, WT + sham vs. AD + anti-PD-L1; $p = 1.000$, WT + control IgG vs. AD + control IgG; $^{*}p = 0.0200$, WT + control IgG vs. AD + anti-PD-L1; $p = 0.9558$, AD + control IgG vs. AD + anti-PD-L1; $^{****}p < 0.0001$, ns, not significant).

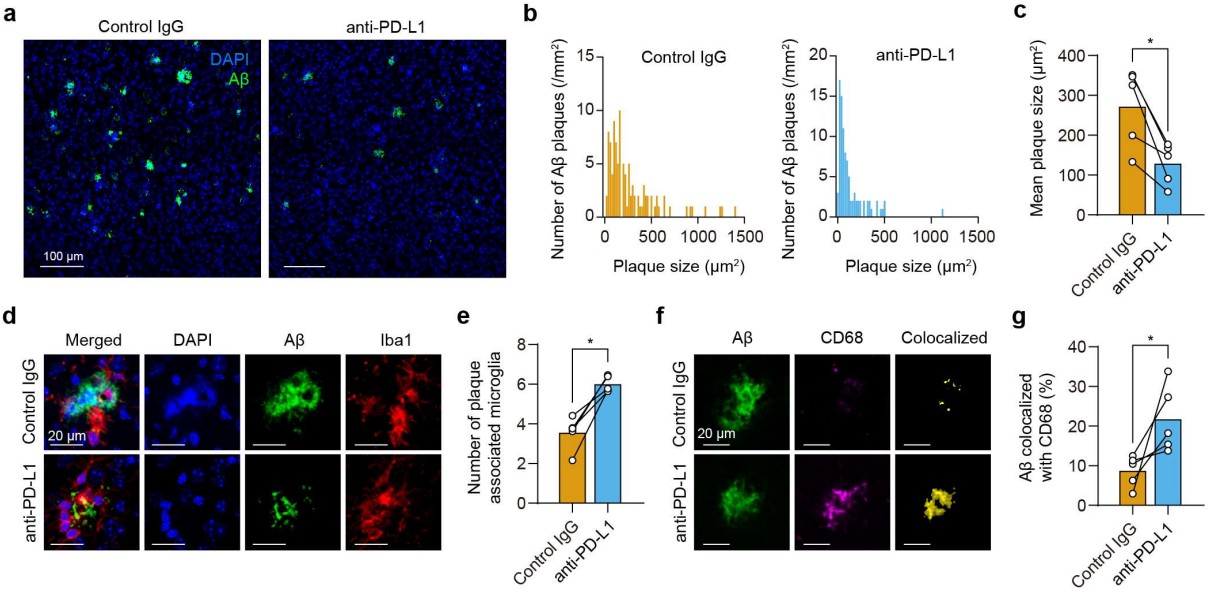

Figure 6. Anti-PD-L1 improves Aβ pathology and promotes microglial phagocytosis in 5xFAD mice.

a, Representative images of control IgG- or anti-PD-L1-injected cortex of 8-month-old 5xFAD mice stained with DAPI (blue) for nuclei and 6E10 (green) for Aβ, assessed at 7 days after single intracortical injection. **b**, Quantitation of the number of Aβ plaques with different sizes (control IgG group; 101 plaques/5 mice, anti-PD-L1 group; 93 plaques/5 mice). **c**, Mean Aβ plaque size in **b** (n = 5 mice, Wilcoxon signed-rank test; *p = 0.043). **d**, Representative images of antibody-injected 5xFAD mice stained with DAPI (blue) for nuclei, 6E10 (green) for Aβ, and Iba1 (red) for microglia. **e**, Quantitation of the number of plaque-associated microglia (n = 5 mice, Wilcoxon signed-rank test; *p = 0.043). **f**, Representative images of antibody-injected cortex of 5xFAD mice stained with 6E10 (green) for Aβ and CD68 (magenta) for a phagocytic phenotype of microglia. Aβ colocalized with CD68 was shown. To examine the colocalization of an Aβ plaque and CD68, z-stacks were acquired and 3D colocalization analysis was conducted using the IMARIS software (Bitplane). **g**, Quantitative assessment of the percentage area of colocalization of Aβ with CD68. Plaques above 300 μm^2 in size were selected for analysis (n = 5 mice, Wilcoxon signed-rank test; *p = 0.043).

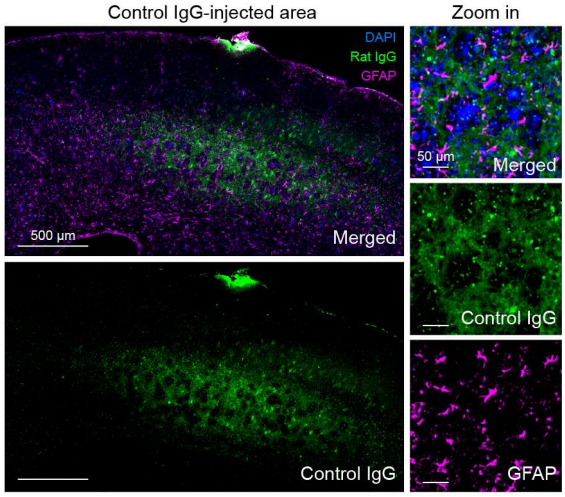

Extended Data Figure 1. Distribution of injected control IgG in the brain of 5xFAD mice.

Representative immunofluorescence images showing astrocytes and injected materials. Immunostaining for GFAP (magenta), tracking the distribution of the control IgG (green) within the S1FL of 8-month-old 5xFAD mice, 1 day after a single intracortical injection (left, 1 µg/µl). The merged images (right), displaying the control IgG (green) and GFAP (magenta).

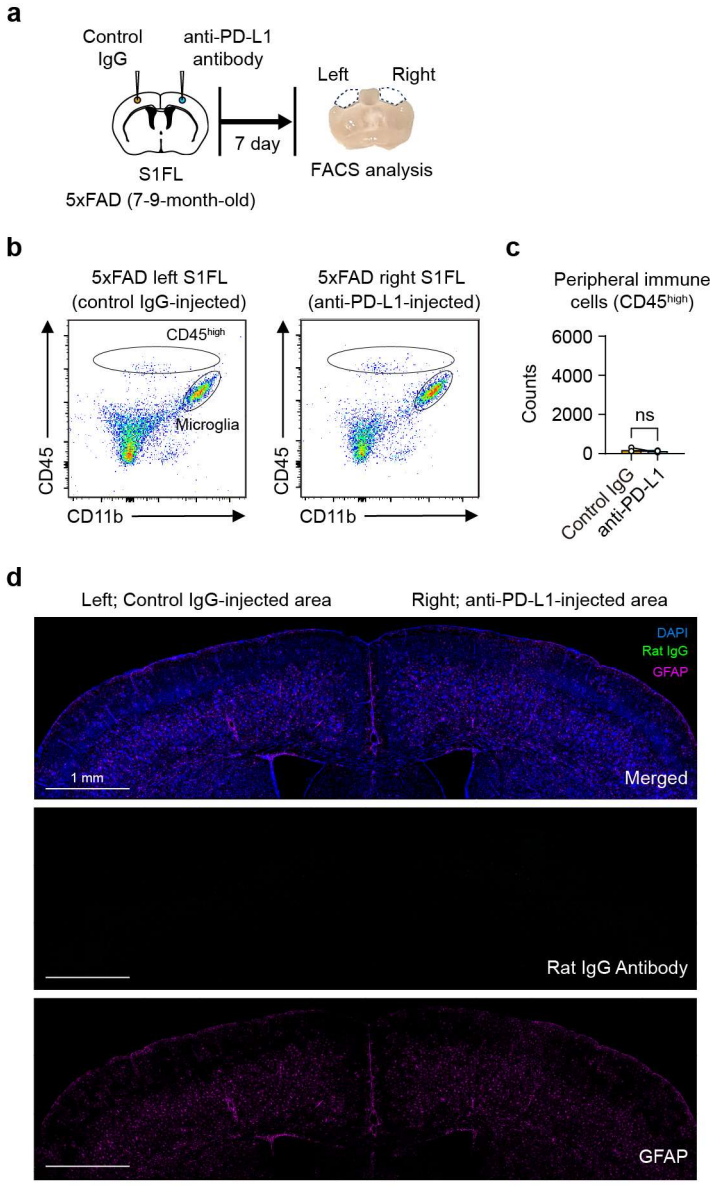

Extended Data Figure 2. Resolution of early immune cell infiltration and absence of injected antibody in the brain of 5xFAD mice by 7 days post-injection.

a, Experimental scheme of flow cytometry analysis of 5xFAD brain tissues by CD11b and CD45 staining in S1FL at 7 days after single intracortical injection. **b**, Representative flow cytometry plots showing peripheral immune cells isolated from the hemispheres of control IgG-injected area (left hemisphere) and anti-PD-L1-injected area (right hemisphere). **c**, Quantification of immune cell infiltration into the brain (n = 5 mice, Wilcoxon signed-rank test; p = 0.225, ns, not significant). **d**, Representative immunofluorescence images showing astrocytes and injected materials. Immunostaining for GFAP tracking the distribution of the control IgG (left hemisphere) and anti-PD-L1 (right hemisphere) within the S1FL of 8-month-old 5xFAD mice, 7 days after a single intracortical injection (1 μg/μl, DAPI; blue, rat IgG; green, GFAP; magenta).

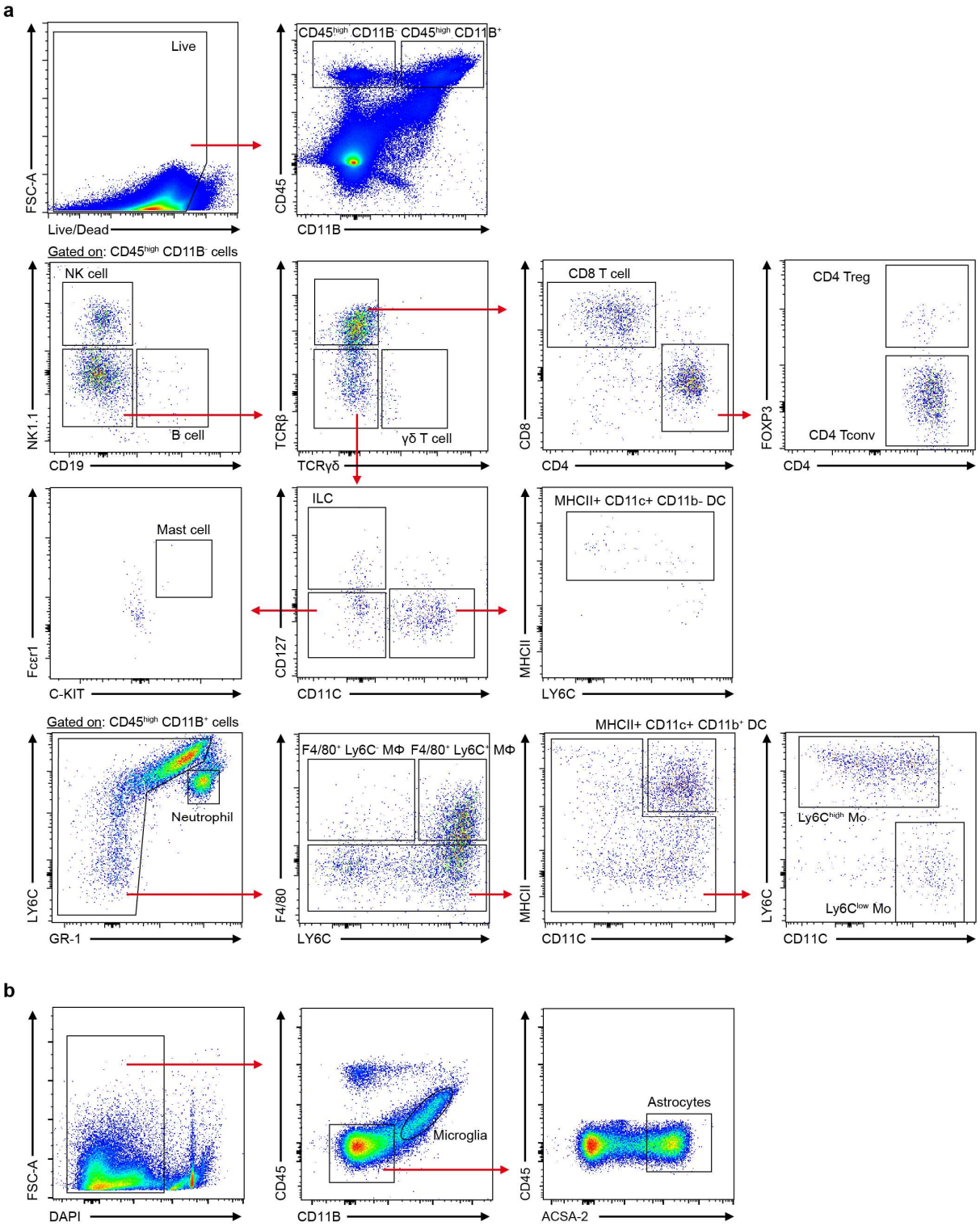

Extended Data Figure 3. Flow cytometry gating strategy used to define cell populations from mouse brain.

a, Gating strategy for flow cytometry analysis of brain-infiltrated immune cells after anti-PD-L1 injection. **b**, Gating strategy for microglia and astrocytes cell sorting.

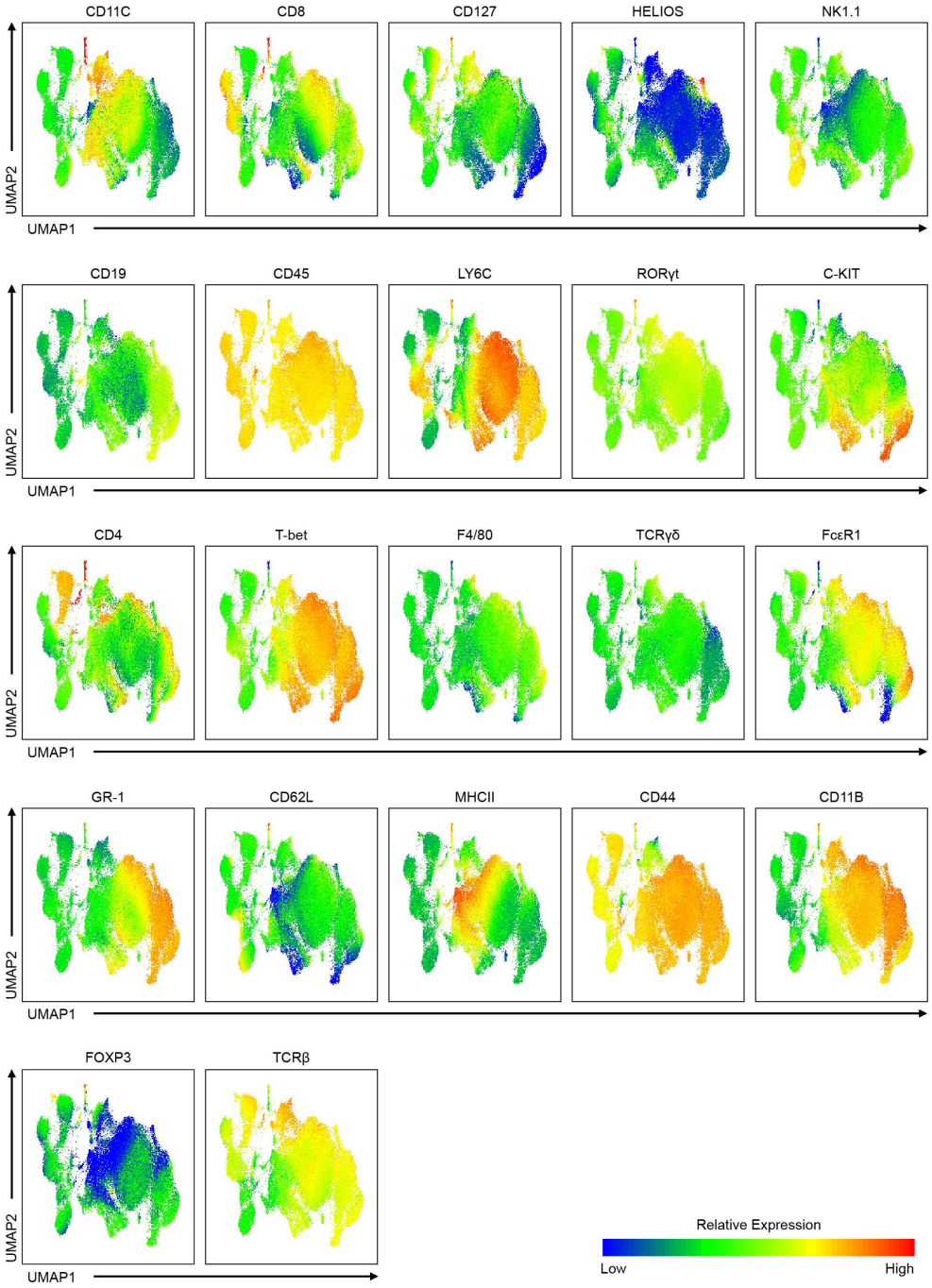

Extended Data Figure 4. UMAP plot showing expression levels of cell-type-specific markers used for flow cytometry analysis.

CD11C; expressed on dendritic cells. CD8; found on cytotoxic T cells. CD127; IL-7 receptor, identifying memory and naïve T cells. HELIOS; A transcription factor linked to regulatory T cells (Treg). NK1.1; a marker for natural killer (NK) cells. CD19; B cell-specific marker. CD45; pan-leukocyte marker, indicative of all hematopoietic cells. LY6C; marker for infiltrating monocytes, which can differentiate into macrophages that assist in tissue repair and debris clearance. RORγt; transcription factor specific to Th17 cells. C-KIT; marker of hematopoietic stem cells and progenitor cells. CD4; expressed on helper T cells, aids in coordinating immune responses. T-bet; transcription factor associated with Th1 cells and cytotoxic T cells. F4/80; a marker for identifying macrophages. TCRγδ; marker for gamma-delta T cells. FcεRI; high-affinity IgE receptor, indicating mast cells and basophils. GR-1; granulocyte marker, typically expressed on neutrophils and monocytes. CD62L; L-selectin, marks naïve and central memory T cells. MHCII; key in antigen presentation, expressed on antigen-presenting cells. CD44; adhesion molecule involved in cell activation and memory T cells. CD11B; expressed on monocytes, macrophages, and neutrophils. FOXP3; transcription factor identifying Treg cells. TCRβ; part of the T cell receptor complex, crucial for antigen recognition by T cells.

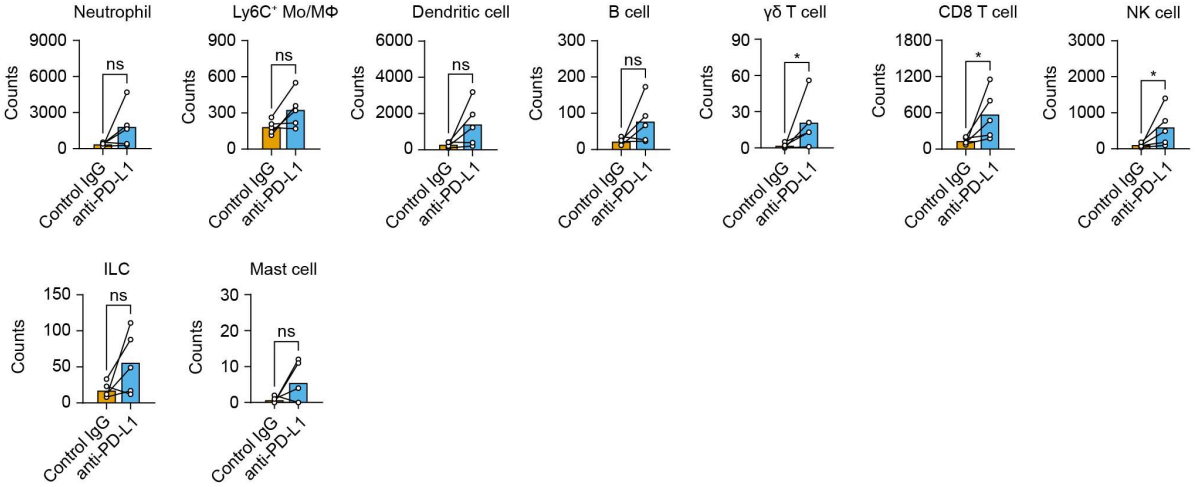

Extended Data Figure 5. Intracortical anti-PD-L1 injection increases the count of brain infiltrating cells in 5xFAD mice.

Counts of brain-infiltrated immune cells in control IgG-injected cortex and anti-PD-L1-injected cortex at 1 day after single intracortical injection ($n = 5$ mice, Wilcoxon signed-rank test; neutrophil; $p = 0.138$, Ly6C$^-$ Mo/MΦ; $p = 0.104$, dendritic cell; $p = 0.080$, B cell; $p = 0.138$, γδ T cell; *$p = 0.043$, CD8 T cell; *$p = 0.043$, NK cell; *$p = 0.043$, ILC; $p = 0.138$, mast cell; $p = 0.144$, ns, not significant).

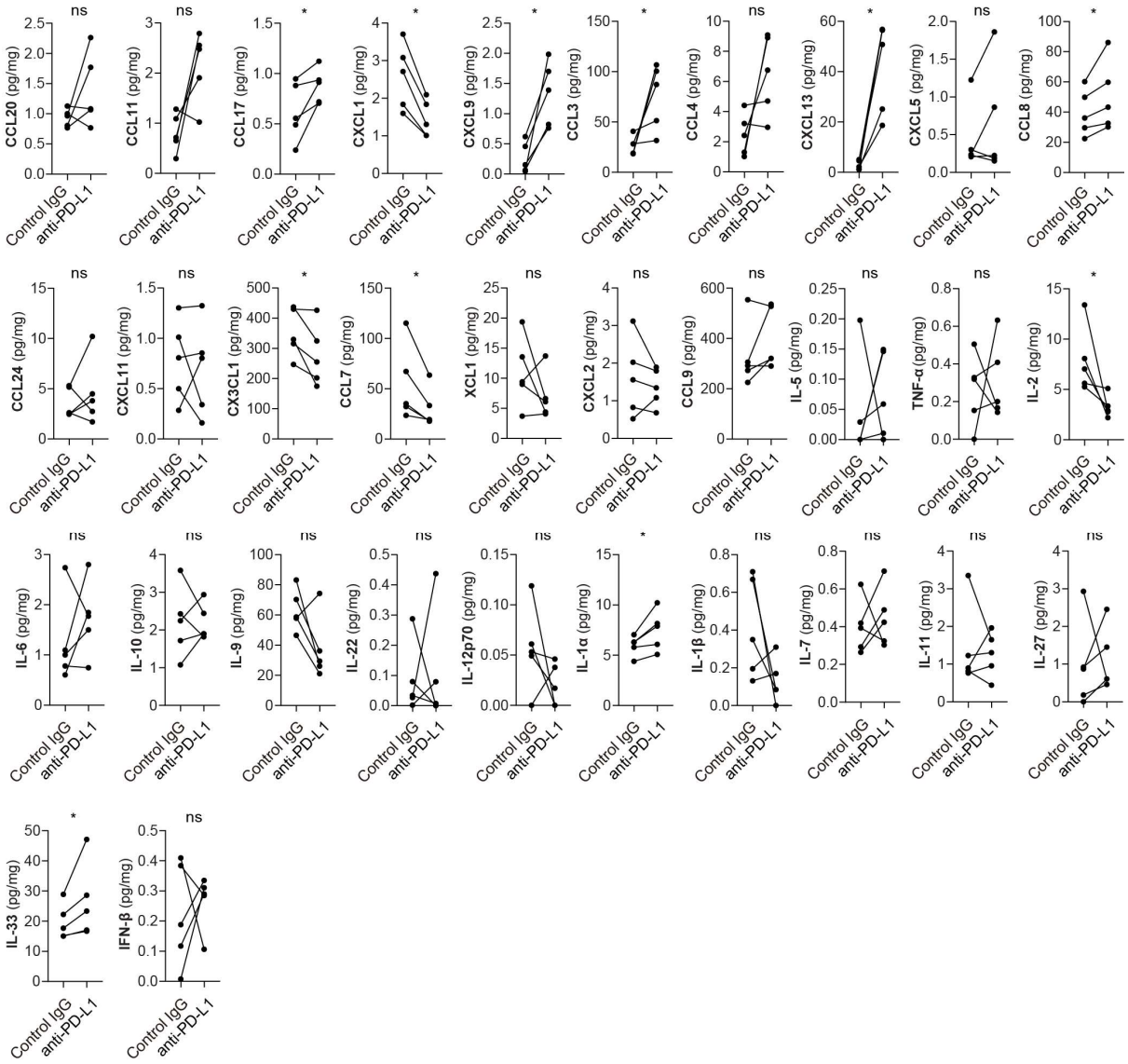

Extended Data Figure 6. Cytokine and chemokine levels at one day after single intracortical injection of control IgG and anti-PD-L1.

Quantification of cytokines and chemokines at 1 day after single intracortical injection of control IgG and anti-PD-L1 (n = 5 mice, Wilcoxon signed-rank test; CCL20; p = 0.225, CCL11; p = 0.080, CCL17; *p = 0.043, CXCL1; *p = 0.043, CXCL9; *p = 0.043, CCL3; *p = 0.043, CCL4; p = 0.080, CXCL13; *p = 0.043, CXCL5; p = 0.500, CCL8; *p = 0.043, CCL24; p = 0.050, CXCL11; p = 0.892, CX3CL1; *p = 0.043, CCL7; *p = 0.043, XCL1; p = 0.345, CXCL2; p = 0.345, CCL9; p = 0.225, IL-5; p = 0.500, TNF-α; p = 0.893, IL-2; *p = 0.043, IL-6; p = 0.345, IL-10; p = 0.893, IL-9; p = 0.080, IL-22; p = 0.893, IL-12p70; p = 0.225, IL-1α; *p = 0.043, IL-1β; p = 0.225, IL-7; p = 0.686, IL-11; p = 0.893, IL-27; p = 0.500, IL-33; *p = 0.043, IFN-β; p = 0.686, ns, not significant).

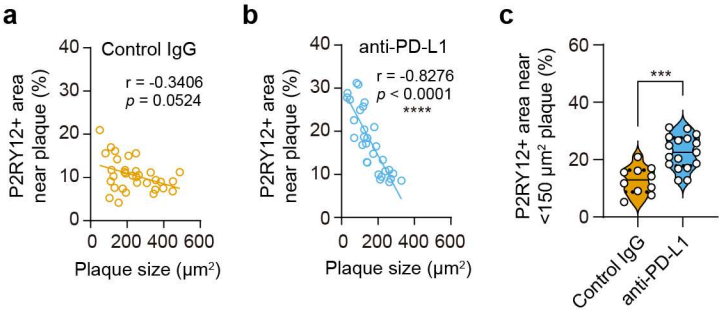

Extended Data Figure 7. Intracortical injection of anti-PD-L1 in 5xFAD mice increases P2RY12-positive area in plaque-associated microglia along with reduction in Aβ plaques.

a, Relationship of the P2RY12 positive area with the plaque size in control IgG-injected area in the 5xFAD mouse (207 plaques, Spearman's r; -0.3406, $p = 0.0524$). **b**, Relationship of the P2RY12 positive area with the plaque size in anti-PD-L1-injected area in the 5xFAD mouse (93 plaques, Spearman's r; -0.8276, ****$p < 0.0001$). **c**, Quantification of P2RY12 positive microglial area surrounding Aβ plaques, each smaller than 150 μm^2 (Control IgG; 10 plaques, anti-PD-L1; 17 plaques, Mann-Whitney U test; ***$p = 0.0003$).

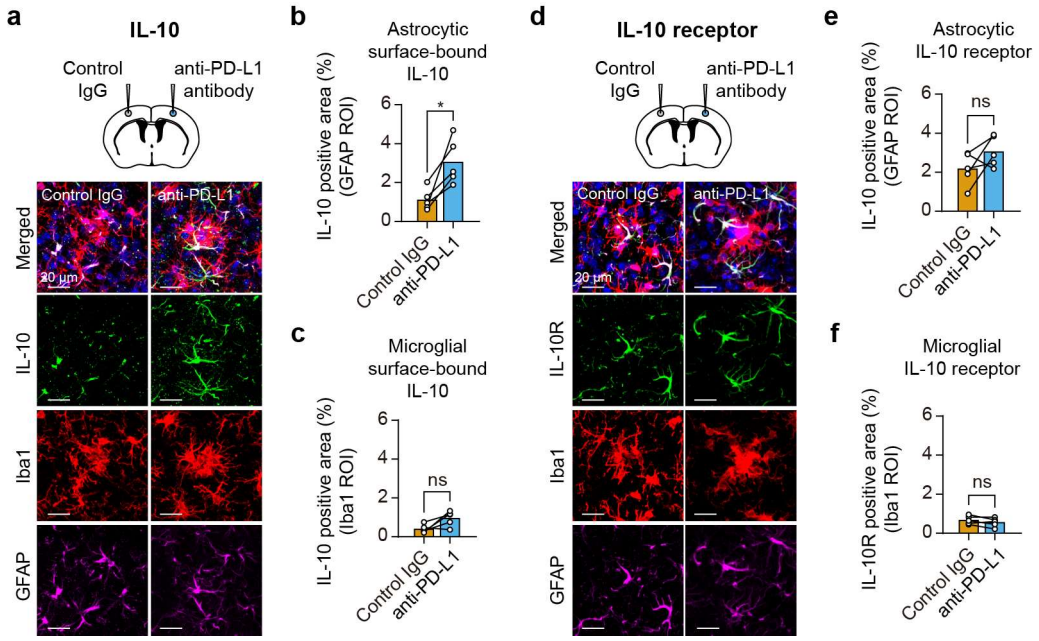

Extended Data Figure 8. Blockade of PD-1/PD-L1 signaling increases astrocytic surface-bound IL-10 in 5xFAD mice brain.

a, Experimental scheme and representative IL-10 immunofluorescence images at 7 days after single intracortical injection (DAPI; blue, IL-10; green, GFAP; magenta, Iba1; red). **b**, Quantitation of the co-localized area of IL-10 and GFAP (n = 5 mice, Wilcoxon signed-rank test; *p = 0.043). **c**, Quantitation of the co-localized area of IL-10 and Iba1 (n = 5 mice, Wilcoxon signed-rank test; p = 0.080, ns, not significant). **d**, Experimental scheme and representative IL-10 receptor (IL-10R) immunofluorescence images at 7 days after single intracortical injection (DAPI; blue, IL-10R; green, GFAP; magenta, Iba1; red). **e**, Quantitation of the co-localized area of IL-10 and GFAP (n = 5 mice, Wilcoxon signed-rank test; p = 0.138, ns, not significant). **f**, Quantitation of the co-localized area of IL-10 and Iba1 (n = 5 mice, Wilcoxon signed-rank test; p = 0.225, ns, not significant).

References

1. Long, J.M. & Holtzman, D.M. Alzheimer disease: an update on pathobiology and treatment strategies. *Cell* **179**, 312-339 (2019).
2. Baruch, K.*, et al.* PD-1 immune checkpoint blockade reduces pathology and improves memory in mouse models of Alzheimer's disease. *Nature medicine* **22**, 135-137 (2016).
3. Rosenzweig, N.*, et al.* PD-1/PD-L1 checkpoint blockade harnesses monocyte-derived macrophages to combat cognitive impairment in a tauopathy mouse model. *Nature communications* **10**, 465 (2019).
4. Chen, S.*, et al.* Macrophages in immunoregulation and therapeutics. *Signal Transduction and Targeted Therapy* **8**, 207 (2023).
5. Prinz, M. & Priller, J. The role of peripheral immune cells in the CNS in steady state and disease. *Nature neuroscience* **20**, 136-144 (2017).
6. Bien-Ly, N.*, et al.* Lack of widespread BBB disruption in Alzheimer's disease models: focus on therapeutic antibodies. *Neuron* **88**, 289-297 (2015).
7. Gustafsson, S., Lindström, V., Ingelsson, M., Hammarlund-Udenaes, M. & Syvänen, S. Intact blood-brain barrier transport of small molecular drugs in animal models of amyloid beta and alpha-synuclein pathology. *Neuropharmacology* **128**, 482-491 (2018).
8. Koronyo, Y.*, et al.* Therapeutic effects of glatiramer acetate and grafted CD115+ monocytes in a mouse model of Alzheimer's disease. *Brain* **138**, 2399-2422 (2015).
9. Lampron, A., Pimentel-Coelho, P.M. & Rivest, S. Migration of bone marrow-derived cells into the central nervous system in models of neurodegeneration. *Journal of Comparative Neurology* **521**, 3863-3876 (2013).
10. Mildner, A.*, et al.* Distinct and non-redundant roles of microglia and myeloid subsets in mouse models of Alzheimer's disease. *Journal of Neuroscience* **31**, 11159-11171 (2011).
11. Chen, X.*, et al.* Microglia-mediated T cell infiltration drives neurodegeneration in tauopathy. *Nature* **615**, 668-677 (2023).
12. Su, W.*, et al.* CXCR6 orchestrates brain CD8+ T cell residency and limits mouse Alzheimer's disease pathology. *Nature immunology* **24**, 1735-1747 (2023).
13. Kummer, M.P.*, et al.* Microglial PD-1 stimulation by astrocytic PD-L1 suppresses neuroinflammation and Alzheimer's disease pathology. *The EMBO journal* **40**, e108662 (2021).
14. Zhao, J.*, et al.* PD-L1/PD-1 checkpoint pathway regulates hippocampal neuronal excitability and learning and memory behavior. *Neuron* **111**, 2709-2726. e2709 (2023).
15. Millet, A., Ledo, J.H. & Tavazoie, S.F. An exhausted-like microglial population accumulates in aged and APOE4 genotype Alzheimer's brains. *Immunity* **57**, 153-170. e156 (2024).
16. Keren-Shaul, H.*, et al.* A unique microglia type associated with restricting development of Alzheimer's disease. *Cell* **169**, 1276-1290. e1217 (2017).
17. Pardoll, D.M. The blockade of immune checkpoints in cancer immunotherapy. *Nature reviews cancer* **12**, 252-264 (2012).
18. Sakuishi, K.*, et al.* Targeting Tim-3 and PD-1 pathways to reverse T cell exhaustion and restore anti-tumor immunity. *Journal of Experimental Medicine* **207**, 2187-2194 (2010).
19. Badimon, A.*, et al.* Negative feedback control of neuronal activity by microglia. *Nature* **586**, 417-423 (2020).
20. Haruwaka, K.*, et al.* Microglia enhance post-anesthesia neuronal activity by shielding inhibitory synapses. *Nature Neuroscience* **27**, 449-461 (2024).
21. Cserép, C.*, et al.* Microglia monitor and protect neuronal function through specialized somatic purinergic junctions. *Science* **367**, 528-537 (2020).
22. Corriveau-Lecavalier, N., Mellah, S., Clément, F. & Belleville, S. Evidence of parietal hyperactivation in individuals with mild cognitive impairment who progressed to dementia: A

894 longitudinal fMRI study. *NeuroImage: Clinical* **24**, 101958 (2019).
895 23. Dickerson, B.*, et al.* Increased hippocampal activation in mild cognitive impairment
896 compared to normal aging and AD. *Neurology* **65**, 404-411 (2005).
897 24. Busche, M.A.*, et al.* Clusters of hyperactive neurons near amyloid plaques in a mouse
898 model of Alzheimer's disease. *Science* **321**, 1686-1689 (2008).
899 25. Minkeviciene, R.*, et al.* Amyloid β-induced neuronal hyperexcitability triggers
900 progressive epilepsy. *Journal of Neuroscience* **29**, 3453-3462 (2009).
901 26. Lerdkrai, C.*, et al.* Intracellular Ca2+ stores control in vivo neuronal hyperactivity in
902 a mouse model of Alzheimer's disease. *Proceedings of the National Academy of Sciences* **115**,
903 E1279-E1288 (2018).
904 27. Yao, J.*, et al.* Limiting RyR2 open time prevents Alzheimer's disease-related neuronal
905 hyperactivity and memory loss but not β-amyloid accumulation. *Cell reports* **32** (2020).
906 28. Mildner, A., Huang, H., Radke, J., Stenzel, W. & Priller, J. P2Y12 receptor is expressed
907 on human microglia under physiological conditions throughout development and is sensitive
908 to neuroinflammatory diseases. *Glia* **65**, 375-387 (2017).
909 29. Kenkhuis, B.*, et al.* Co-expression patterns of microglia markers Iba1, TMEM119 and
910 P2RY12 in Alzheimer's disease. *Neurobiology of disease* **167**, 105684 (2022).
911 30. Maeda, J.*, et al.* Distinct microglial response against Alzheimer's amyloid and tau
912 pathologies characterized by P2Y12 receptor. *Brain Communications* **3**, fcab011 (2021).
913 31. Chen, C.*, et al.* Early impairment of cortical circuit plasticity and connectivity in the
914 5XFAD Alzheimer's disease mouse model. *Translational Psychiatry* **12**, 371 (2022).
915 32. Carlesimo, G.A.*, et al.* Atrophy of presubiculum and subiculum is the earliest
916 hippocampal anatomical marker of Alzheimer's disease. *Alzheimer's & Dementia: Diagnosis,*
917 *Assessment & Disease Monitoring* **1**, 24-32 (2015).
918 33. Liddelow, S.A.*, et al.* Neurotoxic reactive astrocytes are induced by activated
919 microglia. *Nature* **541**, 481-487 (2017).
920 34. Ma, W.*, et al.* Absence of TGFβ signaling in retinal microglia induces retinal
921 degeneration and exacerbates choroidal neovascularization. *Elife* **8**, e42049 (2019).
922 35. Krabbe, G.*, et al.* Functional impairment of microglia coincides with Beta-amyloid
923 deposition in mice with Alzheimer-like pathology. *PloS one* **8**, e60921 (2013).
924 36. Baik, S.H.*, et al.* A breakdown in metabolic reprogramming causes microglia
925 dysfunction in Alzheimer's disease. *Cell metabolism* **30**, 493-507. e496 (2019).
926 37. Gyoneva, S., Swanger, S.A., Zhang, J., Weinshenker, D. & Traynelis, S.F. Altered
927 motility of plaque-associated microglia in a model of Alzheimer's disease. *Neuroscience* **330**,
928 410-420 (2016).
929 38. Condello, C., Yuan, P., Schain, A. & Grutzendler, J. Microglia constitute a barrier that
930 prevents neurotoxic protofibrillar Aβ42 hotspots around plaques. *Nature communications* **6**,
931 6176 (2015).
932 39. Nagele, R.G.*, et al.* Contribution of glial cells to the development of amyloid plaques
933 in Alzheimer's disease. *Neurobiology of aging* **25**, 663-674 (2004).
934 40. Oeckl, P.*, et al.* Glial fibrillary acidic protein in serum is increased in Alzheimer's
935 disease and correlates with cognitive impairment. *Journal of Alzheimer's Disease* **67**, 481-488
936 (2019).
937 41. Pontecorvo, M.J.*, et al.* Association of donanemab treatment with exploratory plasma
938 biomarkers in early symptomatic Alzheimer disease: a secondary analysis of the
939 TRAILBLAZER-ALZ randomized clinical trial. *JAMA neurology* **79**, 1250-1259 (2022).
940 42. Association, A. Revised criteria for diagnosis and staging of Alzheimer's disease:
941 Alzheimer's Association Workgroup. (AAIC, 2023).
942 43. Dionisio-Santos, D.A., Olschowka, J.A. & O'Banion, M.K. Exploiting microglial and

943 peripheral immune cell crosstalk to treat Alzheimer's disease. *Journal of neuroinflammation*
944 **16**, 1-13 (2019).
945 44. Han, R.T., Kim, R.D., Molofsky, A.V. & Liddelow, S.A. Astrocyte-immune cell
946 interactions in physiology and pathology. *Immunity* **54**, 211-224 (2021).
947 45. Jorfi, M.*, et al.* Infiltrating CD8+ T cells exacerbate Alzheimer's disease pathology in
948 a 3D human neuroimmune axis model. *Nature neuroscience* **26**, 1489-1504 (2023).
949 46. Groh, J.*, et al.* Accumulation of cytotoxic T cells in the aged CNS leads to axon
950 degeneration and contributes to cognitive and motor decline. *Nature Aging* **1**, 357-367 (2021).
951 47. Cunningham, C.*, et al.* Systemic inflammation induces acute behavioral and cognitive
952 changes and accelerates neurodegenerative disease. *Biological psychiatry* **65**, 304-312 (2009).
953 48. Yan, P.*, et al.* Peripheral monocyte–derived cells counter amyloid plaque pathogenesis
954 in a mouse model of Alzheimer's disease. *The Journal of clinical investigation* **132** (2022).
955 49. Baek, H.*, et al.* Neuroprotective effects of CD4+ CD25+ Foxp3+ regulatory T cells in
956 a 3xTg-AD Alzheimer's disease model. *Oncotarget* **7**, 69347 (2016).
957 50. Dansokho, C.*, et al.* Regulatory T cells delay disease progression in Alzheimer-like
958 pathology. *Brain* **139**, 1237-1251 (2016).
959 51. Gao, X.*, et al.* PD-L1 signaling in reactive astrocytes counteracts neuroinflammation
960 and ameliorates neuronal damage after traumatic brain injury. *Journal of Neuroinflammation*
961 **19**, 43 (2022).
962 52. Linnerbauer, M.*, et al.* PD-L1 positive astrocytes attenuate inflammatory functions of
963 PD-1 positive microglia in models of autoimmune neuroinflammation. *Nature*
964 *Communications* **14**, 5555 (2023).
965 53. Baruch, K.*, et al.* Breaking immune tolerance by targeting Foxp3+ regulatory T cells
966 mitigates Alzheimer's disease pathology. *Nature communications* **6**, 7967 (2015).
967 54. Heneka, M.T., Kummer, M.P. & Latz, E. Innate immune activation in
968 neurodegenerative disease. *Nature Reviews Immunology* **14**, 463-477 (2014).
969 55. Saraiva, M. & O'garra, A. The regulation of IL-10 production by immune cells. *Nature*
970 *reviews immunology* **10**, 170-181 (2010).
971 56. Norden, D.M., Fenn, A.M., Dugan, A. & Godbout, J.P. TGFβ produced by IL-10
972 redirected astrocytes attenuates microglial activation. *Glia* **62**, 881-895 (2014).
973 57. Shanaki-Bavarsad, M., Almolda, B., González, B. & Castellano, B. Astrocyte-targeted
974 overproduction of IL-10 reduces neurodegeneration after TBI. *Experimental Neurobiology* **31**,
975 173 (2022).
976 58. Kwilasz, A., Grace, P., Serbedzija, P., Maier, S. & Watkins, L. The therapeutic potential
977 of interleukin-10 in neuroimmune diseases. *Neuropharmacology* **96**, 55-69 (2015).
978 59. Tesseur, I.*, et al.* Deficiency in neuronal TGF-β signaling promotes neurodegeneration
979 and Alzheimer's pathology. *The Journal of clinical investigation* **116**, 3060-3069 (2006).
980 60. Heupel, K.*, et al.* Loss of transforming growth factor-beta 2 leads to impairment of
981 central synapse function. *Neural Development* **3**, 1-16 (2008).
982 61. Zhong, H.*, et al.* Neonatal inflammation via persistent TGF-β1 downregulation
983 decreases GABAAR expression in basolateral amygdala leading to the imbalance of the local
984 excitation-inhibition circuits and anxiety-like phenotype in adult mice. *Neurobiology of*
985 *Disease* **169**, 105745 (2022).
986 62. Dobolyi, A., Vincze, C., Pál, G. & Lovas, G. The neuroprotective functions of
987 transforming growth factor beta proteins. *International journal of molecular sciences* **13**, 8219-
988 8258 (2012).
989 63. Wyss-Coray, T.*, et al.* TGF-β1 promotes microglial amyloid-β clearance and reduces
990 plaque burden in transgenic mice. *Nature medicine* **7**, 612-618 (2001).
991 64. Jay, T.R.*, et al.* TREM2 deficiency eliminates TREM2+ inflammatory macrophages

992 and ameliorates pathology in Alzheimer's disease mouse models. *Journal of Experimental*
993 *Medicine* **212**, 287-295 (2015).
994 65. Oakley, H., *et al.* Intraneuronal β-amyloid aggregates, neurodegeneration, and neuron
995 loss in transgenic mice with five familial Alzheimer's disease mutations: potential factors in
996 amyloid plaque formation. *Journal of Neuroscience* **26**, 10129-10140 (2006).
997 66. Jung, S., *et al.* Analysis of fractalkine receptor CX3CR1 function by targeted deletion
998 and green fluorescent protein reporter gene insertion. *Molecular and cellular biology* (2000).
999 67. Schindelin, J., *et al.* Fiji: an open-source platform for biological-image analysis.
1000 *Nature methods* **9**, 676-682 (2012).
1001 68. Lorenzen, A., *et al.* Rapid and direct transport of cell surface APP to the lysosome
1002 defines a novel selective pathway. *Molecular brain* **3**, 1-13 (2010).
1003 69. Umpierre, A.D., *et al.* Microglial calcium signaling is attuned to neuronal activity in
1004 awake mice. *Elife* **9**, e56502 (2020).
1005 70. Busche, M.A., *et al.* Decreased amyloid-β and increased neuronal hyperactivity by
1006 immunotherapy in Alzheimer's models. *Nature neuroscience* **18**, 1725-1727 (2015).
1007 71. Busche, M.A., *et al.* Tau impairs neural circuits, dominating amyloid-β effects, in
1008 Alzheimer models in vivo. *Nature neuroscience* **22**, 57-64 (2019).

1009